J. Fluid Mech. (2024), *vol*. 999, A30, doi:10.1017/jfm.2024.876

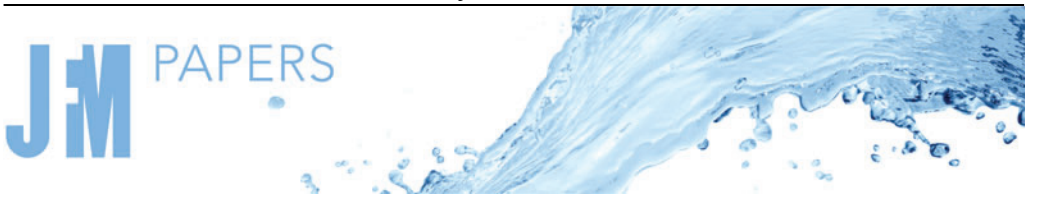

Impacts of inflow turbulence on the flow past a permeable disk

Yunliang Li[1,2], Fengshun Zhang[1,2], Zhaobin Li[1,2] and Xiaolei Yang[1,2,†]

[1]The State Key Laboratory of Nonlinear Mechanics, Institute of Mechanics, Chinese Academy of Sciences, Beijing 100190, PR China

[2]School of Engineering Sciences, University of Chinese Academy of Sciences, Beijing 100049, PR China

(Received 4 March 2024; revised 8 August 2024; accepted 2 September 2024)

A permeable disk serves as a simplified model for the conversion of wind energy by a horizontal axis wind turbine. In this study, we investigate how inflow turbulence intensity (TI), I_∞, and inflow turbulence integral length scale, L_∞, influence the flow recovery in the wake, the capability of a permeable disk in extracting turbulence kinetic energy (TKE) of the incoming flow, and the statistics of wake-added turbulence using large-eddy simulation. The simulated inflows include various TIs (i.e. $I_\infty = 2.5\,\%$–$25\,\%$) and integral length scales (i.e. $L_\infty/D = 0.5$–2.0) for two thrust coefficients. Simulation results show that both inflow TI and integral length scale influence flow recovery via enhanced ejections and sweeps across the wake boundary, with the former strongly affecting the position where the wake starts to recover and the latter mainly on the recovery rate. Moreover, it is shown that increasing I_∞ and L_∞ increases the TKE extraction by the disk, occurring mainly at scales (s) greater than $0.5D$ and frequencies depending on the inflow integral length scale. As for the wake-added TKE, the inflow TI mainly affects its intensity, while the inflow integral length scale affects both its intensity and the sensitive frequencies, with the spectral distributions in scale space (s) being similar and the peak located around $s/D = 1.0$ for the considered inflows.

Key words: wakes, turbulence simulation

1. Introduction

The complexity of wind energy conversion stems from the interplay between the atmospheric turbulent flow and wind turbines and their wakes (Sørensen 2011; Stevens & Meneveau 2017; Meneveau 2019; Veers *et al.* 2019). The atmospheric turbulence happens over a broad range of spatial and temporal scales. Using only turbulence intensity (TI), which is commonly done in wind energy applications, is certainly not enough to

† Email address for correspondence: xyang@imech.ac.cn

describe how atmospheric turbulence affects the energy conversion and wake development for a wind turbine. Several factors, such as terrain and atmospheric stability, affect the characteristics of atmospheric turbulence. This, combined with aerodynamics at the blade scale, makes the study of the impacts of atmospheric turbulence on wind energy conversion rather complicated. A permeable disk, neglecting blade aerodynamics, is often employed in numerical and laboratory experiments to model the aerodynamics of a horizontal axis wind turbine. In this study, we carry out large-eddy simulations (LESs) to investigate the impacts of inflow turbulence intensity and inflow turbulence length scale on the flow past a permeable disk, with focus on flow recovery in the wake, the capability of a disk in extracting inflow turbulence kinetic energy (TKE) and the statistics of wake-added turbulence.

Inflow turbulence affects wind turbine aerodynamics in several aspects. It affects the efficiency of wind energy conversion. In wind tunnel experiments, Gambuzza & Ganapathisubramani (2021) showed that increasing inflow TI increases the power output of a model wind turbine. Such an increase is caused by the dependence of blade aerodynamics on inflow turbulence, especially the flow separation on the suction side of a blade (Talavera & Shu 2017). In the field, on the other hand, complex variations of power output with TI, depending on the wind turbine operation regime and the thermal stratification condition, were observed (St Martin *et al.* 2016). Inflow turbulence affects the wake recovery. In general, the wake recovers faster for higher inflow TIs as shown in wind tunnel experiments (Barlas, Buckingham & van Beeck 2016), numerical simulations (Liu *et al.* 2022) and field measurements (Carbajo Fuertes, Markfort & Porté-Agel 2018). The wake recovery can be described using two parameters, the wake recovery rate and the near wake length. The field measurements by Carbajo Fuertes *et al.* (2018) showed that increasing inflow TI shortens the near wake length and increases the wake recovery rate. Empirical relations were proposed to correlate the expansion coefficient and near wake length with inflow TI (e.g. Bastankhah & Porté-Agel 2016; Carbajo Fuertes *et al.* 2018; Ishihara & Qian 2018; Vahidi & Porté-Agel 2022). It should be noted that the near wake length employed for calculating the growth of the wake width is often not the same as the wind turbine downwind distance for pressure recovery.

Inflow turbulence affects the evolution of coherent flow structures in wind turbine wakes. Both the atmospheric flow and wind turbine wakes consist of flow structures over a broad range of scales, and their interplay affects the wake evolution in different ways. Tip vortices are the typical flow structures in the near-wake region, which separate the low momentum wake flow from the high momentum ambient flow. Ivanell *et al.* (2010) showed that the tip vortex instability is sensitive to inflow perturbations of certain frequencies. Wake meandering, a low-frequency, large-scale motion of wake in the transverse directions, is the dominant flow phenomenon in the far wake. Two mechanisms exist for wake meandering, i.e. the large eddy mechanism and the shear layer instability mechanism. In the first mechanism, inflow eddies with scales greater than a critical scale advect the wake as passive scalars. In the second mechanism, the wake meandering occurring at certain frequencies is similar to vortex shedding from a bluff body. The coexistence of the two mechanisms has been shown in both field measurements and numerical simulations (Heisel, Hong & Guala 2018; Yang & Sotiropoulos 2019). For the first mechanism, it is crucial to define the critical large scale. Our recent work based on energy analysis in scale space showed that the critical scale is around $3D$ (where D is the rotor diameter). As for the second mechanism, it was found that inflow perturbations with frequencies in the range of $0.25 < St < 0.63$ (where $St = fD/U_\infty$) are effective in triggering wake meandering (Mao & Sørensen 2018). A similar range of

frequencies was also observed for the motion of a floating offshore wind turbine, at which a small-amplitude wind turbine motion ($\sim 0.01D$) can trigger wake meandering motion of amplitude in the order of D (Li, Dong & Yang 2022).

The interactions between the inflow turbulence and the wind turbine and its wake are scale-dependent. However, the investigations in this aspect are limited (Chamorro *et al.* 2012; Blackmore, Batten & Bahaj 2014; Jin *et al.* 2016; Gambuzza & Ganapathisubramani 2023), with the TI often being the only metric employed in engineering models (Vermeer, Sørensen & Crespo 2003). In wind tunnel experiments, Chamorro *et al.* (2012) showed that the inflow TKE is reduced at low frequencies when airflow passes a rotor, while the TKE is added at relatively high frequencies in wake, indicating a dual role of a wind turbine as a high-pass filter and an active turbulence generator. In their later experiments for free stream turbulence (Jin *et al.* 2016), it was shown that the TKE is added to a range of frequencies with $0.1 < St < 1.0$ for inflow TI 11.5 %. In recent wind tunnel experiments carried out by Gambuzza & Ganapathisubramani (2023), the impacts of free stream turbulence of both Kolmogorov-like and non-Kolmogorov-like on the wake of a model wind turbine were investigated. Their results showed that the low-frequency velocity fluctuations (with $St \approx 0.01$ and 0.02) in the non-Kolmogorov-like flows are inefficient in promoting the mixing of the wake with the ambient flow. The characteristics of inflow turbulence can be well controlled in numerical simulations. In the LES studies by Blackmore *et al.* (2014) and Ghate *et al.* (2018), it was shown that inflow TI has limited effects on wake width while increasing inflow integral length scale increases wake width (with the inflow TI approximately the same). The above studies shed light on the scale-dependent nature of the 'inflow turbulence'–'wind turbine'–'wake' interactions. However, the detailed dynamics is yet to be investigated for a wide range of parameters. Particularly, the knowledge gaps we attempt to fill in this work are as follows.

(i) Field data showed the dependence of the growth rate of wake width on inflow TI (Carbajo Fuertes *et al.* 2018), without distinguishing the influences of the inflow length scale. The LES results, on the other hand, indicated significant impacts from the inflow length scale on the growth rate (Blackmore *et al.* 2014; Ghate *et al.* 2018). The exact roles of inflow TI and integral length scale on the flow recovery in the wake are missing.

(ii) The wind tunnel experiments by Chamorro *et al.* (2012) showed that a wind turbine acts as a high-pass filter of the inflow turbulence for a particular case. The nature as a filter for different inflow TIs and integral length scales is unclear.

(iii) It has been shown that wake-added TKE is located at a certain range of frequencies for one inflow TI (Jin *et al.* 2016). How the inflow TI and integral length scale impact the spectral characteristics of wake-added TKE is yet to be uncovered.

Numerical simulations, in which the inflow can be specified in a precise way, are effective for investigating how inflow turbulence affects the energy conversion and wake development of a wind turbine. In this work, we employ several simplifications to facilitate the investigation, which cannot be easily done for a utility-scale wind turbine under realistic atmospheric wind conditions. The simplifications include the actuator disk (AD) model without rotation (Yang, Kang & Sotiropoulos 2012) for blade aerodynamics, and the synthetic turbulence technique for generating inflow turbulence with specified TI and turbulence integral length scale. The investigation carried out is of practical importance in developing scale-dependent engineering models, e.g. including both inflow TI and integral length scale in the formulation of the wake expansion model and to describe the wake-added turbulence.

The interaction with the inflow turbulence and the wake for a real-life wind turbine rotor involves a broad range of scales from blade aerodynamics to the atmospheric boundary layer and beyond. The idea of this work is to simplify the problem in order to focus on the impact of the primary role of a wind turbine rotor, i.e. energy extraction, on the scale dynamics. The blade aerodynamics, which is overlooked in this work, should be considered for further analysis of the energy extraction process and dynamics in the near wake. This, however, needs to be done case by case considering various blade designs, which may significantly affect the wake dynamics (Dong *et al.* 2023).

The rest of the paper is structured as follows. In § 2, the numerical method employed is described. Then, the case set-ups are presented in § 3. The obtained results are analysed in § 4. Finally, conclusions are drawn in § 5.

2. Numerical method

Large-eddy simulations are performed using the VFS-Wind code (Yang *et al.* 2015*b*), which has been validated against experiments (Yang & Sotiropoulos 2013; Yang *et al.* 2015*b*; Yang & Sotiropoulos 2018), applied to reveal the mechanism of wind turbine wake (Li & Yang 2021; Dong *et al.* 2023) and wind farm flows (Dong *et al.* 2022; Wang *et al.* 2023) and employed to develop reduced-order models (Li & Yang 2024). In this study, the atmospheric stability condition is set as neutral. The Coriolis force is not considered. In the LES module of the VFS-Wind code, the spatially filtered incompressible Navier–Stokes equations are solved to obtain the flow field, which read as follows:

$$\frac{\partial \tilde{u}_i}{\partial x_i} = 0, \tag{2.1}$$

$$\frac{\partial \tilde{u}_i}{\partial t} + \frac{\partial \tilde{u}_i \tilde{u}_j}{\partial x_j} = -\frac{1}{\rho}\frac{\partial \tilde{p}}{\partial x_i} + \nu \frac{\partial^2 \tilde{u}_i}{\partial x_j \partial x_j} - \frac{\partial \tau_{ij}}{\partial x_j} + f_i, \tag{2.2}$$

where $i, j = 1, 2, 3$ are directional indices, u_i the velocity components, p the pressure, ν the kinematic viscosity, $\tilde{\cdot}$ the spatial-filtering operator and τ_{ij} is the residual stress tensor resulting from the spatial-filtering process. The residual stress tensor τ_{ij} is modelled using an eddy viscosity model as follows:

$$\tau_{ij} - \tfrac{1}{3}\tau_{kk}\delta_{ij} = -2\nu_t \tilde{S}_{ij}, \tag{2.3}$$

where $\tilde{S}_{ij} = (\partial \tilde{u}_i/\partial x_j + \partial \tilde{u}_j/\partial x_i)/2$ is the filtered strain-rate tensor. The eddy viscosity ν_t is calculated by

$$\nu_t = Cs^2 \Delta^2 \left|\tilde{S}\right|, \tag{2.4}$$

where $|\tilde{S}| = \sqrt{2|\tilde{S}_{ij}||\tilde{S}_{ij}|}$, Δ is the filter size and Cs is the Smagorinsky coefficient computed using the dynamic approach (Germano *et al.* 1991). In (2.2), the source term f_i represents the body force resulting from the permeable disk (AD concept) (Yang *et al.* 2012; Yang & Sotiropoulos 2013). In the employed AD model, the thrust of the permeable disk T is uniformly distributed on the disk. The tangential force due to rotor rotation is neglected. The thrust T is computed by specifying the thrust coefficient and using the incoming velocity U_∞ via $T = \frac{1}{2}\rho C_T U_\infty^2 A$, where ρ is the air density and $A = \pi R^2$ (where R is the radius of the AD). In the present implementation of the AD model, the U_∞ is obtained by averaging the instantaneous streamwise velocity over a disk of radius R located at one disk diameter upstream.

		L_∞/D					
I_∞	C_T	0.5	1.0	1.5	0.75	1.25	2.0
2.5 %	0.2	/	✓	/	/	/	/
	0.7	/	✓	/	/	/	∗
10 %	0.2	✓	✓	✓	/	/	/
	0.7	✓	✓	✓	∗	∗	∗
25 %	0.2	✓	✓	✓	/	/	/
	0.7	✓	✓	✓	/	/	/
5.0 %	0.7	∗	∗	∗	/	/	/
15 %	0.7	/	∗	/	/	/	/
17.5 %	0.7	/	/	/	∗	∗	/
20 %	0.7	/	∗	/	/	/	/

Table 1. Case set-up. The ✓ and ∗ denote the simulated cases, in which detailed analyses are carried out for the former.

The governing equations are spatially discretized using the second-order accurate central difference scheme, and the fractional step method is used for the integration in time (Ge & Sotiropoulos 2007). The Jacobian-free Newton–Krylov method (Knoll & Keyes 2004) is used to solve the momentum equation. The pressure Poisson equation is solved using the generalized minimum residuals method with an algebraic multigrid acceleration (Saad 1993).

The inflow turbulence is generated using Mann's method (Mann 1998) which employs the von Kármán spectrum given as follows:

$$E(k) = \alpha\varepsilon^{2/3}L^{5/3}\frac{(Lk)^4}{(1+(Lk)^2)^{17/6}}, \tag{2.5}$$

where k is the wavenumber, L the length scale, α the Kolmogorov constant and ε the rate of viscous dissipation of specific TKE.

The inflow TI and integral length scale (L_∞) are obtained by tuning the two parameters (i.e. ε and L.) in (2.5).

3. Case set-up

We consider three TIs and three integral length scales (L_∞) for the inflow, with two different permeable disk thrust coefficients (C_T), resulting in a total of 25 different cases, listed in table 1. The employed computational domain and the probes for collecting time series of velocities are shown in figure 1. The size of the computational is $L_x \times L_y \times L_z = 16D \times 8D \times 8D$ with the corresponding grid number $N_x \times N_y \times N_z = 256 \times 128 \times 128$, where x, y and z denote the streamwise, spanwise and vertical directions, respectively. A uniform mesh with $\Delta x = D/16$, $\Delta y = D/16$ and $\Delta z = D/16$ is employed.

The Courant–Friedrichs–Lewy number is 0.64. The permeable disk is located at $3D$ downstream of the inlet plane. The periodic boundary condition is applied in the transverse directions. At the outlet, the Neumann boundary condition is employed. At the inlet, a uniform velocity is superposed with the velocity fluctuations generated using Mann's method.

Each case is run for 32 flow-throughs, including approximately one flow-through to achieve a fully developed state and approximately 31 flow-throughs for computing flow statistics. As the inflow velocity is uniform, there is no mechanism to maintain turbulence,

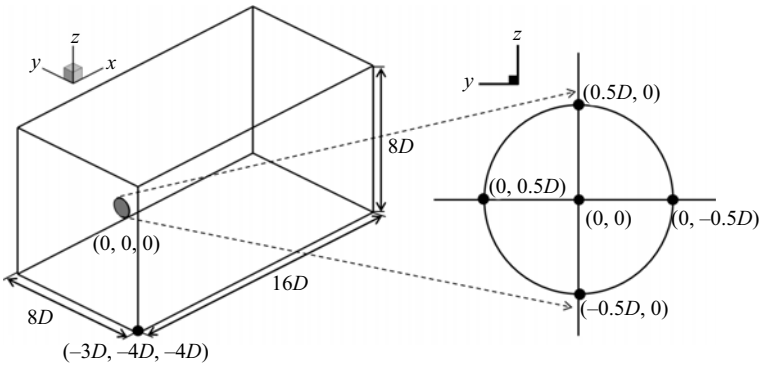

Figure 1. Schematic of the computational domain employed in the work and how the time series of velocity are extracted. The values are extracted for the marked dots.

then the turbulence decays in the downstream direction. To separate the inflow turbulence decay from the wake development, a simulation without a disk is conducted for each inflow. When calculating the flow statistics, the azimuthal averaging at four sampled points along the edge is further carried out whenever possible to increase the number of samples.

In addition to the dynamic model, the Smagorinsky model with $C_S = 0.1$ and the Lagrangian dynamic model (Meneveau, Lund & Cabot 1996) were tested. The results show (not shown in the paper) that the differences in the velocity deficit and the TKE predicted by the three subgrid scale models are negligible, which was also shown in the literature (Sarlak, Meneveau & Sørensen 2015; Martinez-Tossas *et al.* 2018). The dependence of the predictions on grid resolution was also tested for $\Delta x = \Delta y = \Delta z = D/10$, $D/16$, $D/20$. The results show (not shown in the paper) that the velocity deficits and the wake-added TKE in the shear layer are not sensitive to the grid resolution. The TKE reduction in the very near wake, on the other hand, is observed being sensitive to the grid resolution for the lowest inflow TI cases. However, considering that the TKE reduction is not dominant for the low inflow TI cases, which is approximately two orders of magnitude lower for the $I_\infty = 2.5\,\%$ case in comparison with the $I_\infty = 25\,\%$ case. The employed grid resolution is considered to be adequate for the present study.

4. Results

In this section, we analyse the simulation results focusing on velocity deficits ($\Delta\bar{u}$), wake-added TKE (Δk), premultiplied spectra of TKE ($f\Phi_k = f(\Phi_u + \Phi_v + \Phi_w)$, where Φ_u, Φ_v and Φ_w are the power spectral densities (PSDs) of velocity fluctuations, and energy density in scale space. One particular focus of the analysis is on mean kinetic energy (MKE), K_m, and TKE, k, which are defined as

$$K_m = \tfrac{1}{2}\left(\bar{u}^2 + \bar{v}^2 + \bar{w}^2\right), \tag{4.1}$$

$$k = \tfrac{1}{2}\left(\overline{u'^2} + \overline{v'^2} + \overline{w'^2}\right), \tag{4.2}$$

where $\bar{\cdot}$ denotes the averaging in time. The velocity deficits and wake-added TKE are calculated relative to the velocity and TKE obtained from corresponding simulations without a disk. The Δg is defined as $\Delta g = g_D - g_{noD}$ where g_D and g_{noD} are quantities from the cases with and without the permeable disk, respectively. The $\langle\cdot\rangle_D$ denotes the averaging over a circular disk of radius R.

The time-averaged thrust and power (i.e. $\bar{T}$ and $\bar{P}$) are first examined in figure 2, which are normalized by the corresponding values from the case with uniform inflow (i.e. T_0 and P_0). As seen, the differences are less than 3 % and 2 % for $\bar{T}$ and $\bar{P}$, respectively, indicating that the impacts of variations in $\bar{T}$ and $\bar{P}$ on the wake dynamics are negligible. The instantaneous flow fields for several typical cases are demonstrated. Specifically, the snapshots at three consecutive instants are shown in figures 3 and 4 for varying inflow turbulence intensities and length scales, respectively. The mean streamwise velocity at the inlet is subtracted to show better the velocity fluctuations. A two-dimensional box filter of width $0.5D$ is employed to obtain the filtered streamwise velocity. The filtered velocity fluctuation fields from the cases with different inflow TIs are shown in figure 3. It is seen that the wake boundary is distorted at far wake locations ($5D$–$6D$ permeable disk downwind) for the low inflow TI case. When the inflow TI is high, on the other hand, intense interactions between the wake and the ambient flow happen right after the disk. It is observed in figure 4 that the interaction between the inflow turbulence and the wake depends on the inflow turbulence length scale: (i) when the inflow length scale is smaller (i.e. $L_\infty/D = 0.5$), the wake is longer with its boundary distorted by the ambient turbulence; (ii) when the inflow length scale is larger (i.e. $L_\infty/D = 1.5$), the wake is shorter and modulated as a whole by the inflow eddy with relatively smooth wake boundaries. Animations showing the temporal variations of the filtered instantaneous flow fields can be found in the supplemental files (Movie 1 and Movie 2) available at https://doi.org/10.1017/jfm.2024.876. The interaction between the inflow turbulence and the wake flow is further examined by analysing 12 400 snapshots using the snapshot proper orthogonal decomposition (POD) method (Sirovich 1987).

The first five POD modes for the cases with different inflow TIs and different inflow length scales are shown in figures 5 and 6, respectively. It is seen in figure 5 that the first five most energetic modes are mainly from the wake flow when inflow TI $I_\infty = 2.5\,\%$, while are dominated by the inflow turbulence when the inflow TI $I_\infty = 25\,\%$. The inflow length scale affects the patterns of the dominant POD modes. For the same inflow TI, the intensity of the wake-induced POD patterns is greater than that of the ambient flow when the inflow length scale $L_\infty/D = 0.5$, while it can be considered as perturbance to the inflow modes for the first three POD modes when the inflow length scale $L_\infty/D = 1.5$. The POD results are consistent with the observations in the instantaneous flow fields (figures 3 and 4), providing another aspect on the qualitative understanding of the space–time characteristics of velocity fluctuations.

Before systematically analysing the impacts of the inflow TI and integral length scale on the statistics of velocity fluctuations, the maximum TKE reduction (which appears in the immediate downstream of the disk) and wake-added TKE in the tip shear layer for the simulated cases are shown in figures 7(*a*) and 7(*b*), respectively, to show an overall picture of the interaction between the inflow turbulence and the wake flow. It is seen that the maximum TKE reduction increases when increasing L_∞ and I_∞ of the inflow. The maximum wake-added TKE increases with the increase of L_∞, while decreases with the increase of I_∞. It should be noted that the variations of the maximum TKE deficit and the maximum TKE increase shown in the figure are not caused by the variations in thrust, which are less than 3 % (shown in figure 2) and cannot cause the considerable variations shown in figure 7.

4.1. *Influences of inflow TI*

In this section, we examine the influence of inflow TI, which is of the same integral length scale (L_∞) of $1.0D$, on the energy conversion and wake statistics of a permeable disk.

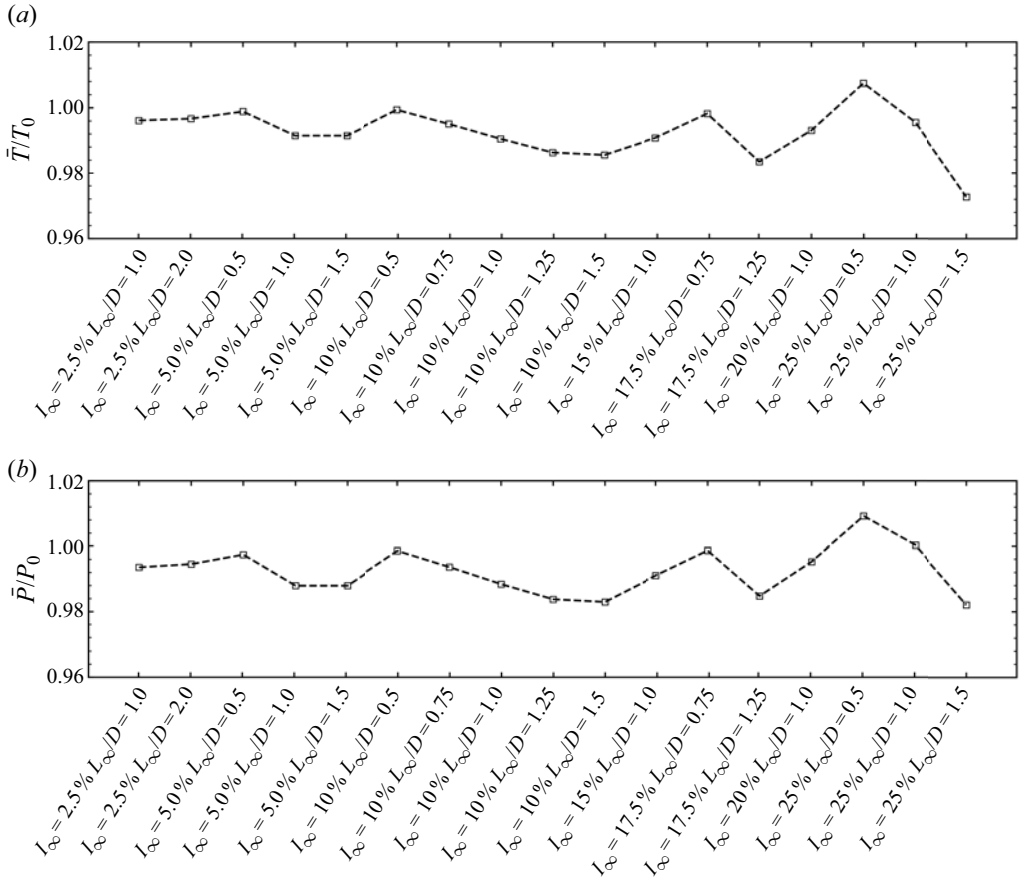

Figure 2. (*a*) Normalized time-averaged thrust of the permeable disk. (*b*) Normalized time-averaged power of the permeable disk. The thrust coefficient $C_T = 0.7$.

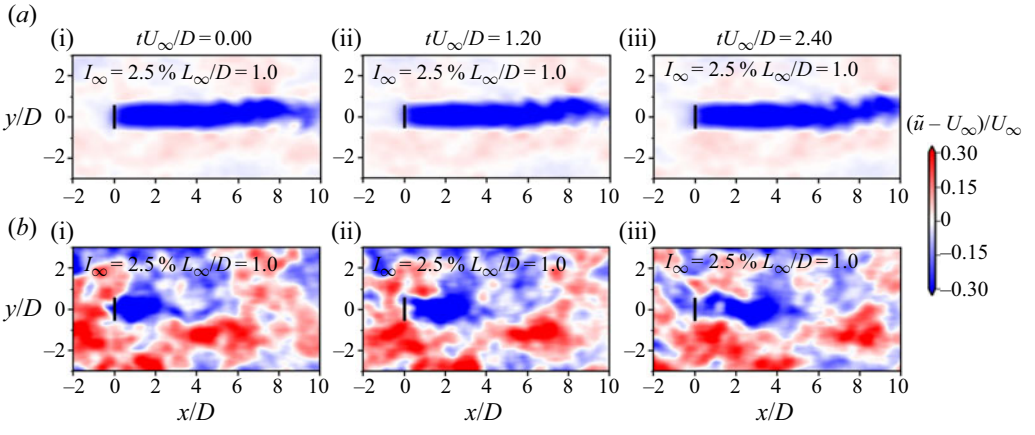

Figure 3. Contours of filtered streamwise velocity fluctuations (the mean streamwise velocity at the inlet is subtracted) at three consecutive instants for different inflow TIs. Here (*a* i–iii) $I_\infty = 2.5\,\%$; (*b* i–iii) $I_\infty = 25\,\%$ with the inflow length scale $L_\infty/D = 1.0$ and the thrust coefficient $C_T = 0.7$.

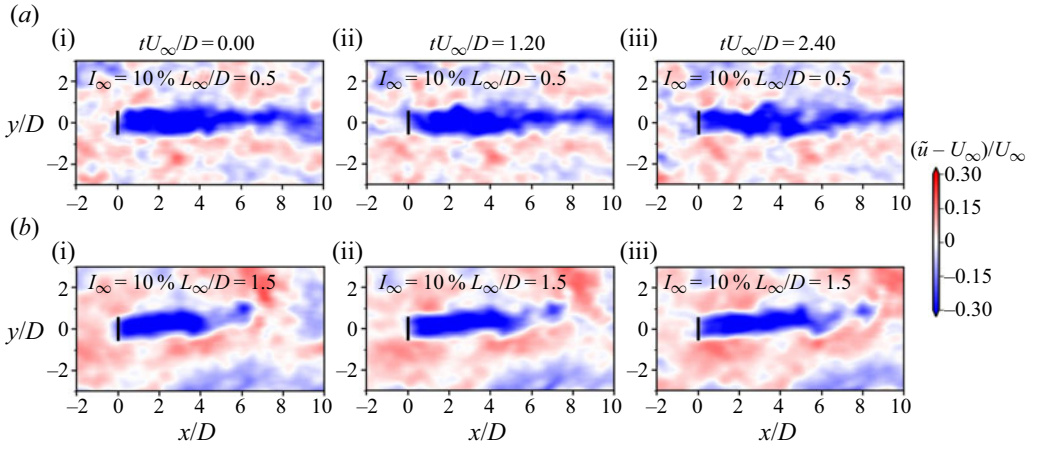

Figure 4. Contours of filtered streamwise velocity fluctuations (the mean streamwise velocity at the inlet is subtracted) at three consecutive instants for different inflow length scales. Here (*a* i–iii) $L_\infty/D = 0.5$; (*b* i–iii) $L_\infty/D = 1.5$ with the inflow TI $I_\infty = 10\,\%$ and the thrust coefficient $C_T = 0.7$.

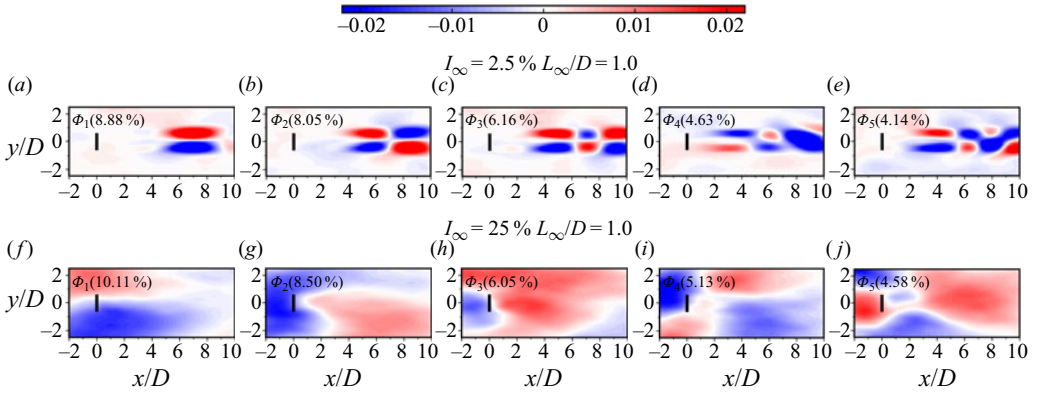

Figure 5. Contours of the first five POD modes of the filtered streamwise velocity normalized by U_∞ (the percentage in parentheses represents the proportion of modal energy). Panels (*a–e*) for $I_\infty = 2.5\,\%$, (*f–j*) for $I_\infty = 25\,\%$ with the inflow length scale $L_\infty/D = 1.0$ and the thrust coefficient $C_T = 0.7$. The solid black lines represent the permeable disk.

4.1.1. *Time-averaged flow statistics*

When flow goes past a permeable disk, part of the inflow MKE, TKE and the potential energy in pressure are extracted. In the wake of the disk, the pressure restores, the MKE recovers and the TKE first increases and then decays. To investigate how inflow TI affects the above process, the downstream variations of the normalized temporal and disk-averaged (along wake centreline with radius of rotor radius R) MKE difference $\langle \Delta K_m \rangle_D / U_\infty^2$, TKE difference $\langle \Delta k \rangle_D / U_\infty^2$ and pressure difference $\langle \Delta \bar{p} \rangle_D / U_\infty^2$ relative to the corresponding non-permeable disk case are plotted in figure 8 for the considered inflow turbulence intensities.

It is seen that the energy extracted by the permeable disk is mainly converted from MKE and potential energy in pressure, with a small percentage from TKE. With the increase of the inflow TI, the part converted from MKE decreases and the TKE part increases. It is interesting to notice that the pressure drops are almost the same for different inflow TIs

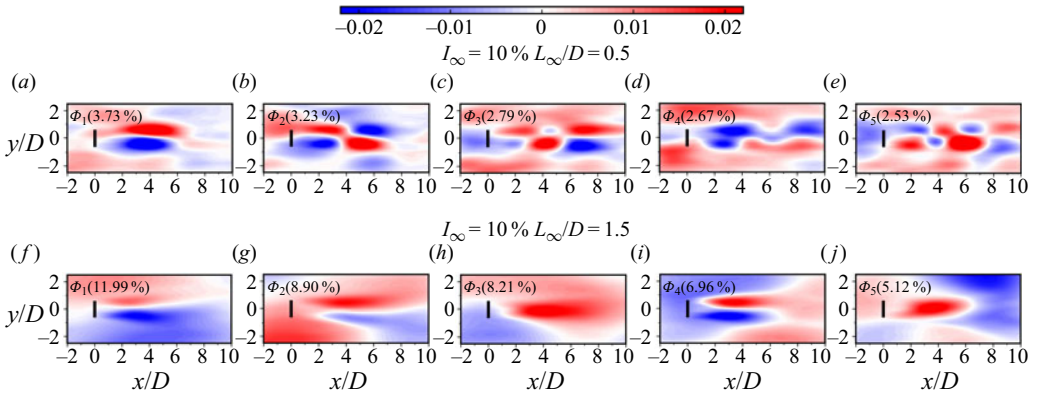

Figure 6. Contours of the first five POD modes of the filtered streamwise velocity normalized by U_∞ (the percentage in parentheses represents the proportion of modal energy). Panels (*a–e*) for $L_\infty/D = 0.5$, (*f–j*) for $L_\infty/D = 1.5$ with the inflow TI $I_\infty = 10\,\%$ and the thrust coefficient $C_T = 0.7$. The solid black lines represent the permeable disk.

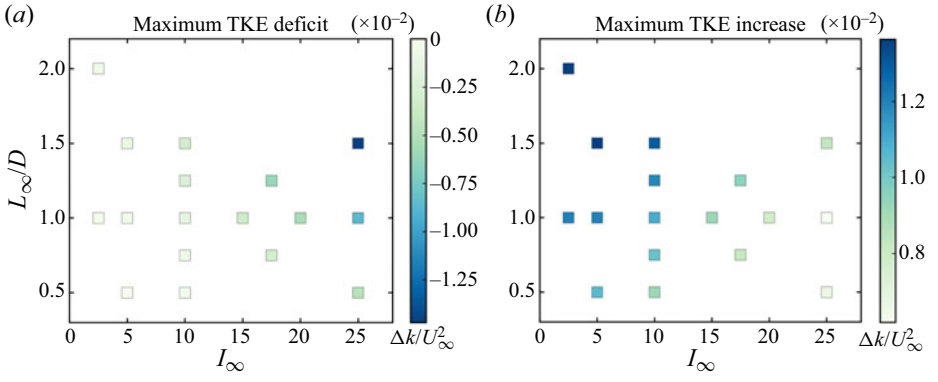

Figure 7. Maximum disk-extracted TKE (*a*) and maximum wake-added TKE (*b*) along the wake centreline and the edge of the permeable disk, respectively, for various inflow turbulence intensities (I_∞) and integral length scales (L_∞).

for both C_T. As expected, the MKE recovers at a faster rate for a higher inflow TI. As for $\langle \Delta k \rangle_D$, the position of the maximum peaks is located closer to the permeable disk for a higher inflow TI.

After showing the energy conversion process for different inflow TIs, in the following we examine the statistics of the mean wake. Figure 9 shows contours of the time-averaged streamwise velocity deficit ($\Delta\bar{u}$) on the x–y plane passing through the rotor centre. The downstream variations of the velocity deficit along the wake centreline are shown in figure 10 for the simulated cases. It is seen that the evolution of maximum velocity deficit approximately follows a power law starting from a certain disk downstream position. The inflow TI affects the starting position of flow recovery in the wake and the recovery rate, being closer to the disk and of a higher value for a higher inflow TI. An overall higher wake recovery rate is observed when C_T is larger. This is because the momentum entrainment due to the wake shear layer is higher for a larger C_T, with that due to the ambient turbulence being the same.

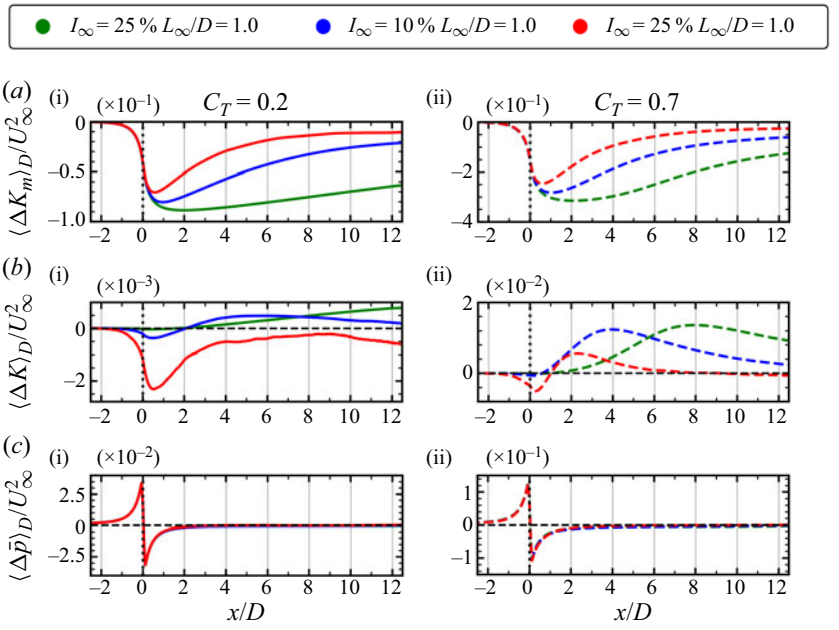

Figure 8. Time- and disk-averaged MKE difference $\langle \Delta K_m \rangle_D / U_\infty^2$ (*a* i,ii), TKE difference $\langle \Delta k \rangle_D / U_\infty^2$ (*b* i,ii) and pressure difference $\langle \Delta \bar{p} \rangle_D$ (*c* i,ii). The dashed black line represents the zero reference line. Here $C_T = 0.2$ (solid lines) and $C_T = 0.7$ (dashed lines).

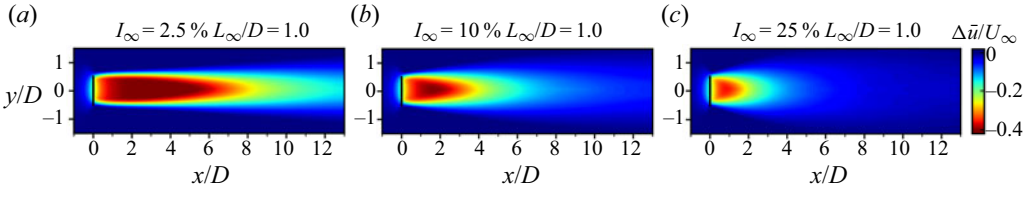

Figure 9. Contours of time-averaged streamwise velocity deficits ($\Delta \bar{u}/U_\infty$) in the spanwise plane passing through the permeable disk centre at $C_T = 0.7$: (*a*) $I_\infty = 2.5\,\%$; (*b*) $I_\infty = 10\,\%$; (*c*) $I_\infty = 25\,\%$. The solid black lines represent the permeable disk.

Figure 11 shows the variations of wake half-width ($R_{1/2}$) along the downstream direction, which is defined as the distance from the wake centre where velocity deficit is half of the maximum value. As seen, the wake expands from a position closer to the permeable disk when the inflow TI is higher. A larger wake expansion rate is not observed for a higher inflow TI, possibly because the intensity of momentum entrainment is not always positively correlated with the inflow TI, as reported by Kankanwadi & Buxton (2020). As for the effect of C_T, the wake's half-width is greater and the wake starts expansion earlier for $C_T = 0.7$ when compared with $C_T = 0.2$. To better understand the trends demonstrated in figures 10 and 11, the reference scaling from the two limiting cases, i.e. (i) the wake shear layer serves as the cause for the flow recovery, with the ambient flow being non-turbulent, and (ii) the wake considered as a passive scalar advected by the ambient turbulence are added. The scaling laws can be obtained using the dimensional analysis and the conservation of momentum (Lissaman 1979; Schlichting & Gersten 2016). It is seen that the trends from the LES cases are located between the scaling laws from the

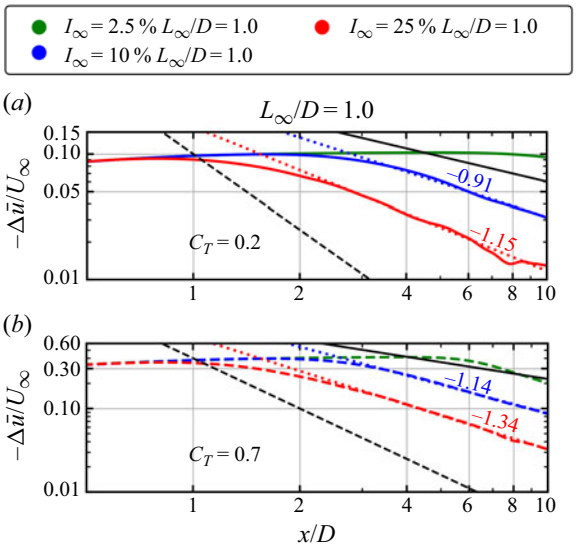

Figure 10. Streamwise variations of the streamwise velocity deficits along disk centreline for (*a*) $C_T = 0.2$ (solid lines) and (*b*) $C_T = 0.7$ (dashed lines) for different inflow turbulence intensities. The solid ($\sim x^{-2/3}$) and dashed ($\sim x^{-2}$) black lines represent the two limit cases: (i) the ambient flow is non-turbulent, and the wake shear layer is the cause for flow recovery, and (ii) the wake is considered as a passive scalar with the ambient turbulence as the cause for flow recovery, respectively.

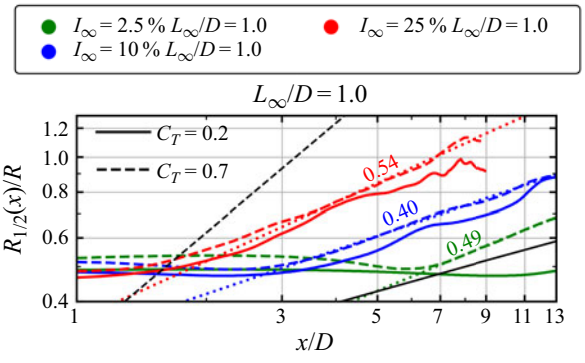

Figure 11. Streamwise variations of the time-averaged wake half-width $R_{1/2}$ for different inflow turbulence intensities. $C_T = 0.2$, solid lines; $C_T = 0.7$, dashed lines. The solid ($\sim x^{1/3}$) and dashed ($\sim x$) black lines represent the two limit cases: (i) the ambient flow is non-turbulent, and the wake shear layer is the cause for flow recovery, and (i) the wake is considered as a passive scalar with the ambient turbulence as the cause for flow recovery, respectively.

two limit cases. The goodness of the fitting of the exponents for the velocity deficit and wake width is shown in Appendix A.

To probe into the mechanism for flow recovery in the wake, various terms in the MKE budget equation are analysed as in the literature (Meyers & Meneveau 2013; Yang *et al.* 2015*a*; Cortina, Calaf & Cal 2016; Ge *et al.* 2020). Specifically, the MKE budget equation integrated over the y–z plane is employed to analyse the variations of various terms in the downstream direction. The integration starts from $y_1 = y_c - R$ to $y_2 = y_c + R$ and $z_1 = z_c - R$ to $z_2 = z_c + R$ in the transverse directions, with y_c and z_c the coordinates of

the wake centreline. The employed MKE budget equation is in the following form:

$$\underbrace{\int_{y1}^{y2}\int_{z1}^{z2}\frac{\partial \overline{u_i}\,\overline{u_i}/2}{\partial t}\,\mathrm{d}y\,\mathrm{d}z}_{=0} = \int_{y1}^{y2}\int_{z1}^{z2}\Bigg\{\underbrace{-\overline{u_j}\frac{\partial \overline{u_i}\;\overline{u_i}/2}{\partial x_j}}_{\text{mean convection }(C_m)}$$
$$\underbrace{-\frac{\partial\left(\bar{p}\,\overline{u_j}/\rho\right)}{\partial x_j}}_{\text{pressure transport }(P_t)}\quad\underbrace{-\frac{\partial\left(\overline{u_i'u_j'}\,\overline{u_i}\right)}{\partial x_j}}_{\text{turbulence convection }(C_t)}\quad\underbrace{+2\frac{\partial\,(\nu+\nu_t)\,S_{ij}\overline{u_i}}{\partial x_j}}_{\text{diffusion }(D_f)}$$
$$\underbrace{+\overline{u_i'u_j'}\frac{\partial \overline{u_i}}{\partial x_j}}_{\text{turbulence production}(T_p)}\quad\underbrace{-2\,(\nu+\nu_t)\,S_{ij}\frac{\partial \overline{u_i}}{\partial x_j}}_{\text{dissipation}(D_p)}\underbrace{+\overline{f_i}\,\overline{u_i}}_{W_D}\Bigg\}\,\mathrm{d}y\,\mathrm{d}z. \tag{4.3}$$

Since the considered case is statistically steady, the time derivative term on the left-hand side is zero after averaging the momentum equation in time. The various terms on the right-hand side are the mean convection (C_m), pressure transport (P_t), turbulence convection (C_t), diffusion (D_f), turbulence production (T_p), dissipation (D_p) and the work done by the permeable disk (W_D) (Wu & Porté-Agel 2012; Abkar & Porté-Agel 2015). The integration operation is included for various terms in the above equation in the presented results, although each term is labelled in the curly braces with the integration operation placed outside.

In figure 12, we focus on the analysis of the turbulence production (P_t), pressure transport (T_p), turbulence convection (C_t) and mean convection (C_m) terms. The W_D + Res term (*Res* stands for residual) is shown in figure 12(*e*), which is negligible at most locations except near the disk where the magnitude of the W_D term is large. It is seen that the inflow TI mainly affects the P_t, C_t and C_m terms, in a way that the magnitudes of the peaks become larger with the corresponding streamwise locations located closer to the disk for higher inflow TIs. The T_p terms, on the other hand, are approximately the same for different inflow TIs. From the MKE analysis, it is clear that the faster recovery of MKE for higher inflow TI is achieved by allocating the region with a high C_t term to near-wake locations and by enhancing the intensity of the C_t term.

After showing the downstream variation of MKE, in the following, we examine wake-added TKE (Δk). In figure 13, we show contours of Δk on the x–y plane pass through the wake centreline. As seen, the TKE is increased along the wake edge because of the existence of the wake shear layer. With the increase of inflow TI, the location for the maximum Δk is located closer to the disk, with its magnitude decreasing especially for TI from 10 % to 25 %. One important observation is that Δk becomes negative in the near-wake region for high TIs, indicating that a part of TKE is extracted by the permeable disk. For $C_T = 0.2$, Δk is negative for a long range of wake when $I_\infty = 25\,\%$. A quantitative comparison of Δk is shown in figure 14 for the two values of C_T.

4.1.2. *Spectral analysis*

To understand how turbulent fluctuations of different scales are affected by a permeable disk and its wake, we carry out spectral analysis in both frequency space and scale space.

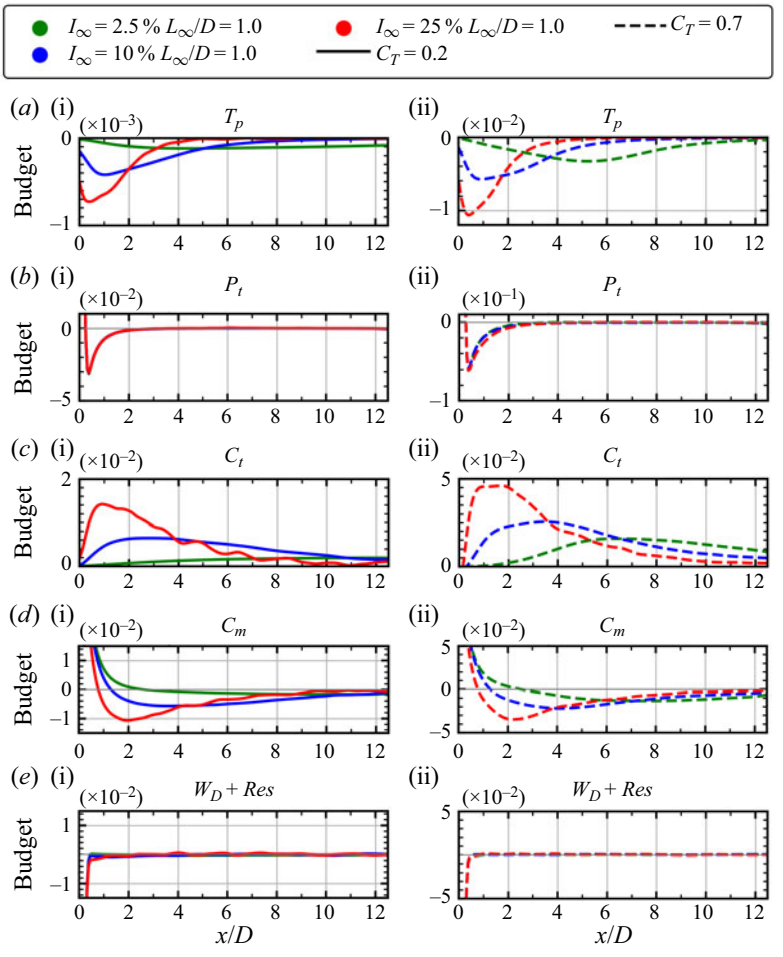

Figure 12. (*a* i,ii) Turbulence production (T_p), (*b* i,ii) pressure transport (P_t), (*c* i,ii) turbulence convection (C_t), (*d* i,ii) mean convection (C_m) and (*e* i,ii) W_D + Res terms in the MKE budget equation for different inflow TIs, in which subpanels (i) are for $C_T = 0.2$ (solid lines) and subpanels (ii) are for $C_T = 0.7$ (dashed lines). The MKE budget terms are normalized using U_∞ and D.

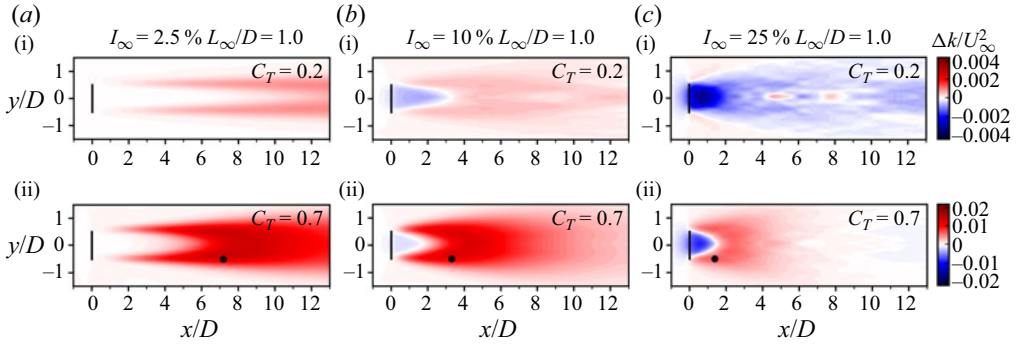

Figure 13. Contours of wake-added TKE (Δk) on the x–y plane passing through wake centreline for different inflow TIs: (*a* i,ii) $I_\infty = 2.5\,\%$, (*b* i,ii) $I_\infty = 10\,\%$, (*c* i,ii) $I_\infty = 25\,\%$. The solid black lines represent the permeable disk. The black dots indicate the positions with the maximum wake-added TKE at the edge region of the permeable disk. Here solid lines, $C_T = 0.2$; dashed lines, $C_T = 0.7$.

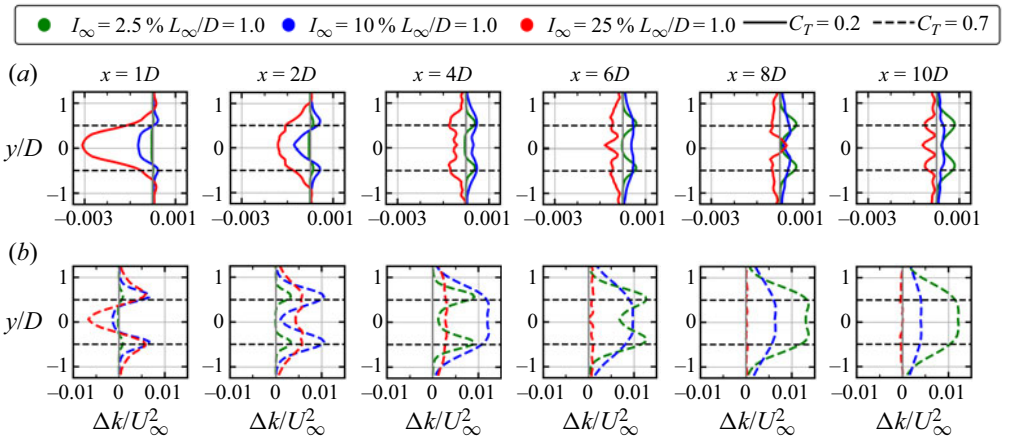

Figure 14. Comparison of transverse profiles of wake-added TKE (Δk) at various disk downstream locations for different inflow TIs for (*a*) $C_T = 0.2$ (solid lines), (*b*) $C_T = 0.7$ (dashed lines). The horizontal black dotted lines at $y/D = \pm 0.5$ are the tip locations.

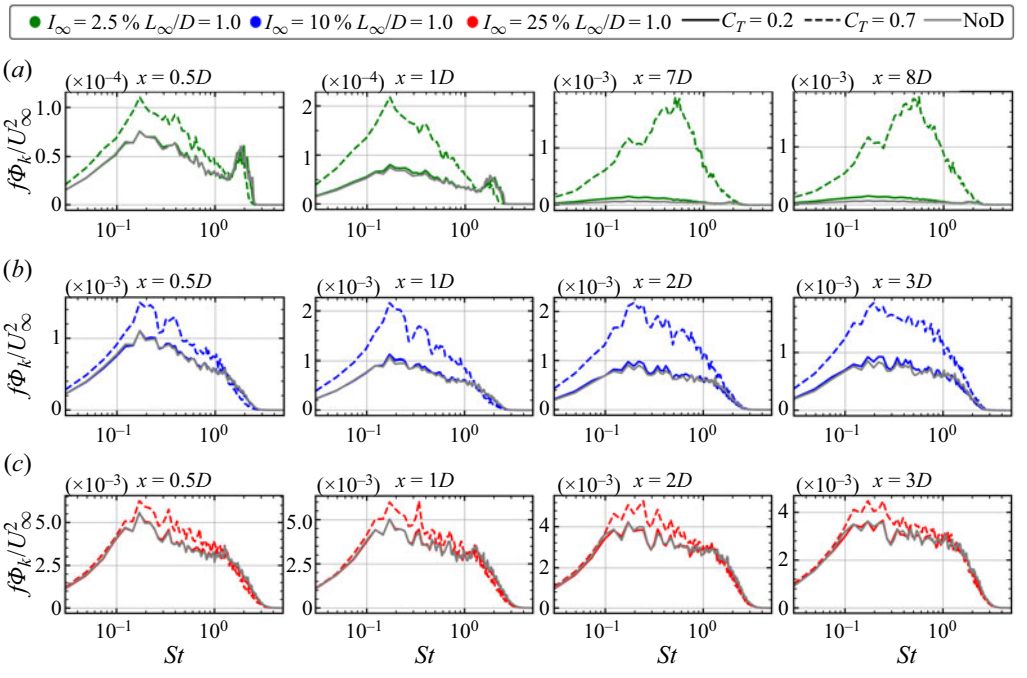

Figure 15. Premultiplied PSD of TKE along disk edge at various disk downstream locations for different inflow TIs. Here (*a*) $I_\infty = 2.5\,\%$; (*b*) $I_\infty = 10\,\%$; (*c*) $I_\infty = 25\,\%$. Here solid lines, $C_T = 0.2$; dashed lines, $C_T = 0.7$; grey lines, cases without a disk.

We first show the premultiplied spectra of TKE ($f\Phi_k$) along the edge of the disk to probe into how a disk adds turbulence to ambient flow in figure 15. The Strouhal number (St) is defined based on the disk diameter and the inflow wind speed. The most important observation is that the range of frequencies affected by a disk wake depends on the inflow TI, being wider for lower inflow TI. Specifically, a significant amount of TKE can be added

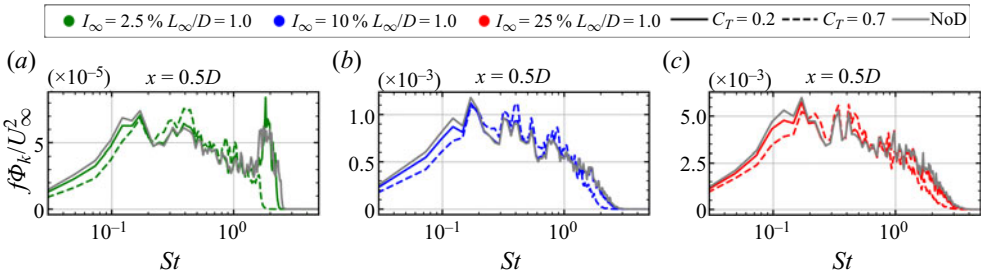

Figure 16. Premultiplied PSD of TKE along wake centreline at various disk downstream locations for different inflow TIs. Here (*a*) $I_\infty = 2.5\,\%$; (*b*) $I_\infty = 10\,\%$; (*c*) $I_\infty = 25\,\%$. Here solid lines, $C_T = 0.2$; dashed lines, $C_T = 0.7$; grey lines, cases without a disk.

to $St < 2.0$, $St < 1.5$ and $0.1 < St < 1.0$ for $I_\infty = 2.5\,\%$, $10\,\%$ and $25\,\%$, respectively. Dependence on C_T is observed as well – that the disk becomes almost incapable of adding TKE to the wake when C_T is small and the inflow TI is high.

The premultiplied spectra of TKE ($f\Phi_k$) along the disk centreline are examined in figure 16. As expected, the downstream variations of $f\Phi_k$ are different from that along the disk edge, because of the time taken for the shear layer around the edge to expand and meet at the centre. One focus here is to examine the range of frequencies at which TKE is extracted by the disk. It is observed from $f\Phi_k$ at a $0.5D$ disk downstream that such TKE reduction mostly happens at relatively low frequencies with $St < 0.15$ and relatively high frequencies with $St > 1.5$, respectively.

After the examination of TKE variations in frequency space, we analyse how TKE of different scales is extracted by the disk and added by the wake by decomposing velocity fluctuations in scale space using the method proposed in our previous work (Zhang, Yang & He 2023). In the employed approach, the decomposition of velocity fluctuations in scale space is carried out using a sphere-averaged filter. In this study, the sphere-averaged filtering is conducted on the x–y plane at the disk centre, that the velocity fluctuations larger than and smaller than the filter scale (s), i.e. $u_i'^{,s>}$ and $u_i'^{,s<}$, are computed as follows:

$$u_i'^{,s>}(x, y) = f * u_i'(x, y) = \int_{-\infty}^{+\infty}\int_{-\infty}^{+\infty} f(x - x', y - y')u_i'(x', y')\,\mathrm{d}x'\,\mathrm{d}y', \tag{4.4}$$

$$u_i'^{,s<}(x, y) = (1 - f) * u_i'(x, y) = u_i'(x, y) - u_i'^{,s>}(x, y), \tag{4.5}$$

where $f(r_d, s)$ is the kernel function defined as

$$f(r_d, s) = \frac{\epsilon\left(\dfrac{s}{2} - r_d\right)}{C_d s^d}, \tag{4.6}$$

in which $r_d = \sqrt{\sum_{i=1}^{d}(x_i - x_i')^2}$.

With the velocity decomposition in scale space, the corresponding energy density can be computed as follows:

$$E(x, s) = -\frac{\partial Q}{\partial s}, \tag{4.7}$$

where $Q = \frac{1}{2}\langle u_i'^{,s>} u_i'^{,s>}\rangle$ is the TKE calculated using the filtered velocity fluctuations.

Since the inflow TKE decays in the downstream direction, we plot the energy density difference between the cases with and without a disk. Figure 17 shows the contours of

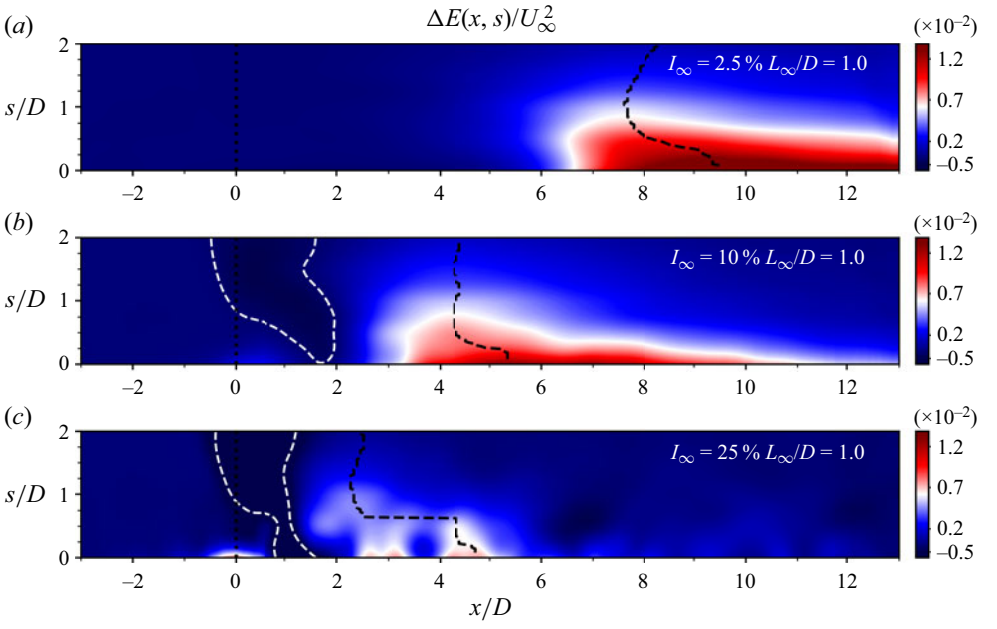

Figure 17. Contours of energy density difference $\Delta E(x, s)$ on the x–s plane for (*a*) $I_\infty = 2.5\,\%$, (*b*) $I_\infty = 10\,\%$ and (*c*) $I_\infty = 25\,\%$, respectively, for $C_T = 0.7$ and $L_\infty/D = 1.0$ cases. The white dashed line corresponds to 0.25 times of the maximum of TKE reduction. The black dashed line is the peak of energy density in the streamwise location for each scale. The vertical black dotted line indicates the permeable disk position.

energy density difference ΔE on the x–s plane for different inflow TIs. The extraction of TKE in the near wake is clearly demonstrated. At low inflow TI (i.e. $I_\infty = 2.5\,\%$ for this work), no TKE extraction happens. For the two high inflow TIs (i.e. $I_\infty = 10\,\%, 25\,\%$), similar patterns are observed indicating two types of TKE extraction. The first one is governed by the disk. The second one happens in the near wake as the pressure restores to the inflow level. The first one mainly happens at large scales, while the second one happens at a much wider range of scales. Increase in TKE occurs at farther downstream locations. It is seen that changing inflow TI influences the distribution of ΔE over s. For low inflow TI (e.g. $I_\infty = 2.5\,\%$), ΔE is concentrated at small scales (e.g. $s/D < 0.5$ for $I_\infty = 2.5\,\%$), which is spread over a wide range of scales for high inflow TI (e.g. $s/D < 1.5$ for $I_\infty = 25\,\%$). One interesting observation is that, the TKE of large scales arrives the peak earlier than that of small scales, being consistent with the energy cascade process. The critical scale separating the large and small scales is approximately in the range of $0.3D$ to $0.6D$, being larger for $I_\infty = 25\,\%$.

The premultiplied energy density differences at various disk streamwise positions are examined in figure 18. It is seen that the disk is capable of extracting inflow TKE for scales greater than approximately $0.5D$, with slight changes in the critical scale when the inflow TI increases from 10 % to 25 %, and the peak is located around $2.0D$. The TKE added by the wake, on the other hand, is mainly located for scales less than $3D$, with slight decreases in the critical scale when the inflow TI increases from 2.5 % to 25 %, and the peak is located around $1.0D$.

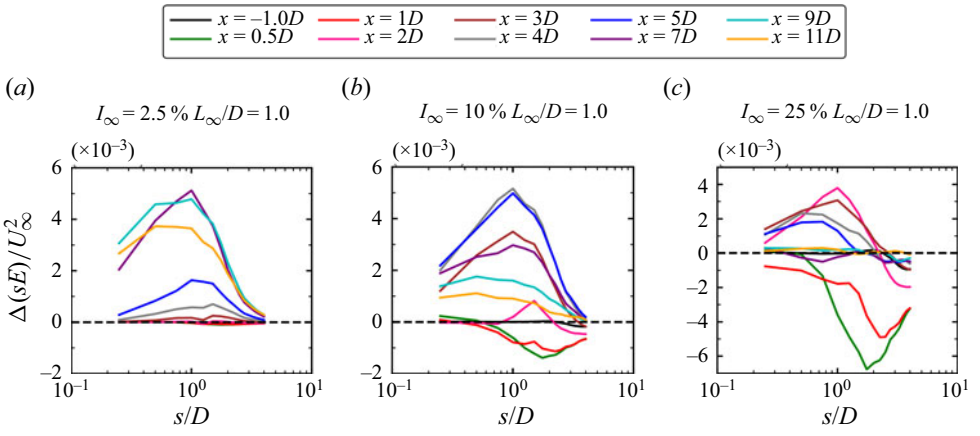

Figure 18. Premultiplied energy density difference (ΔsE) in scale space (s) at different streamwise locations for cases with different inflow TIs for (a) $I_\infty = 2.5\,\%$, (b) $I_\infty = 10\,\%$ and (c) $I_\infty = 25\,\%$ with $L_\infty = 1.0D$ and $C_T = 0.7$.

4.1.3. *Quadrant analysis*

The quadrant analysis (Wallace, Eckelmann & Brodkey 1972; Wallace 2016) is carried out to probe into the influences of inflow on the interaction of wake with the ambient flow. The events in the four quadrants are outward interactions in quadrant 1 ($Q1$), ejections in quadrant 2 ($Q2$), inward interactions in quadrant 3 ($Q3$) and sweeps in quadrant 4 ($Q4$). The ejection and sweep events in $Q2$ and $Q4$ (where velocity fluctuations in the streamwise and the radial directions are of opposite signs), represent the gradient-type motions, being the main contribution to the Reynolds shear stress, $\overline{u_a' u_r'}$ (where the subscripts $\cdot_a$ and $\cdot_r$ denote the axial and radial directions, respectively). They are often counteracted by the interaction quadrants in $Q1$ and $Q3$ (where velocity fluctuations in the two directions are of the same sign) for shear flows. The analyses are focused on their contributions to the Reynolds shear stress and are conducted for cases with and without the permeable disk, such that the wake effects can be examined. The contributions from the four quadrants to the Reynolds shear stress are denoted as S_1, S_2, S_3 and S_4 and are calculated according to (4.9). They correspond to events $Q1$, $Q2$, $Q3$ and $Q4$, respectively, with ΔS_1, ΔS_2, ΔS_3, ΔS_4 being the wake-added contributions. The ΔS_1, ΔS_2, ΔS_3, ΔS_4 are examined in two ways: (i) normalized using the incoming velocity for comparisons between various cases; (ii) normalized using $\sum_{i=1}^{4} S_i$ to show their relative contributions to the Reynolds shear stress as (4.9). The definitions for S_i and ΔS_i are given as follows:

$$S_i = \left(\overline{u_a' u_r'}\right)_i, \tag{4.8}$$

where $i = 1, 2, 3, 4$ for quadrants $Q_{1,2,3,4}$, respectively, and

$$\Delta S_i = (S_i)_D - (S_i)_{noD}\,, \tag{4.9}$$

where the subscripts D and noD are for the results with and without a disk, as defined.

The quadrant analysis results for cases with different inflow TIs are shown in figures 19 and 20. As seen in figure 19(i), all the four quadrants contribute positively to the Reynolds shear stress, being different from those observed in the wall-bounded turbulent flows for which the S_1 and S_3 are negative. This is understandable because of the isotropic turbulent inflow, for which the four quadrants contribute equally. In figure 19(ii), it is seen that the

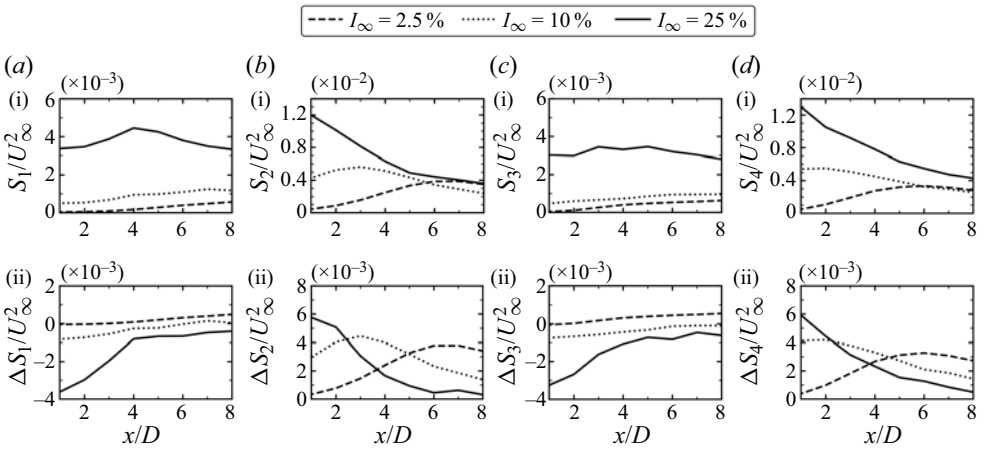

Figure 19. Quadrant analysis for cases with different inflow TIs for (*a* i,*b* i,*c* i,*d* i) contributions in each quadrant (S_i/U_∞^2), (*a* ii,*b* ii,*c* ii,*d* ii) wake-added difference in each quadrant ($\Delta S_i/U_\infty^2$). The inflow integral length scale is $L_\infty/D = 1.0$. The thrust coefficient is $C_T = 0.7$.

ΔS_1 and ΔS_3 are negative, indicating that the wake reduces the $Q1$ and $Q3$ contributions to the Reynolds shear stress. Such reductions are greater in the near wake and increases with the increase in inflow TI. As expected, the wake enhances the ejections and sweeps in $Q2$ and $Q4$, making them the dominant events for the generation of Reynolds shear stress and the flow recovery in the wake. With the increase in inflow TI, the maximum of ΔS_2 and ΔS_4 increases, with the corresponding position moving upstream to the permeable disk. As for the relative contributions, it is seen that the relative contributions in $Q2$ and $Q4$ are comparable with each other, and their sum decreases with the increase in inflow TI.

4.2. *Influences of inflow turbulence length scale*

In this section, we investigate how inflow turbulence length scales affect the extraction of TKE by the disk and the addition of TKE by the wake. Simulation results from three integral length scales, i.e. $L_\infty/D = 0.5$, 1.0, 1.5 are compared for two inflow TIs, i.e. $I_\infty = 10\,\%$ and $25\,\%$ and two thrust coefficients $C_T = 0.2$ and 0.7.

4.2.1. *Time-averaged flow statistics*

The time- and disk-averaged $\langle \Delta K_m \rangle_D$, $\langle \Delta k \rangle_D$ and ΔP_D are first examined in figure 21. It is seen that the inflow turbulence length scale affects both the peaks and the corresponding positions of $\langle \Delta K_m \rangle_D$ and $\langle \Delta k \rangle_D$. Compared with inflow TI, the impacts of inflow L_∞ are mainly found on the magnitudes of peaks. When increasing the inflow L_∞, the maximum MKE reduction decreases, with the differences between cases with different L_∞ more pronounced for higher inflow TI. The inflow turbulence length scale L_∞ influences the TKE peaks in the other way, that the maximum TKE reduction and the maximum TKE addition increase with L_∞. This is reasonable as the disk is more capable of extracting TKE at larger scales. Being the same as the observation for different inflow TIs, changing inflow L_∞ does not affect the streamwise variation of pressure.

The downstream evolution of mean wake is examined in this part.

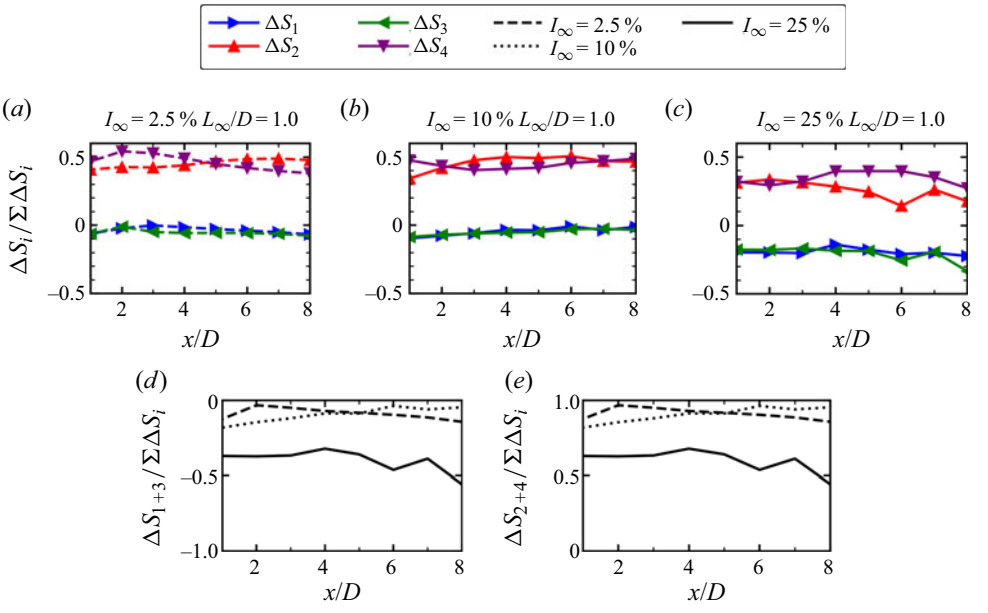

Figure 20. (*a–c*) Wake-added relative contributions in each quadrant ($\Delta S_i/\sum \Delta S_i$); (*d*) wake-added relative contributions in $Q1$ and $Q3$ events; (*e*) wake-added relative contributions in $Q2$ and $Q4$ events with different inflow TIs. The inflow integral length scale is $L_\infty/D = 1.0$. The thrust coefficient is $C_T = 0.7$.

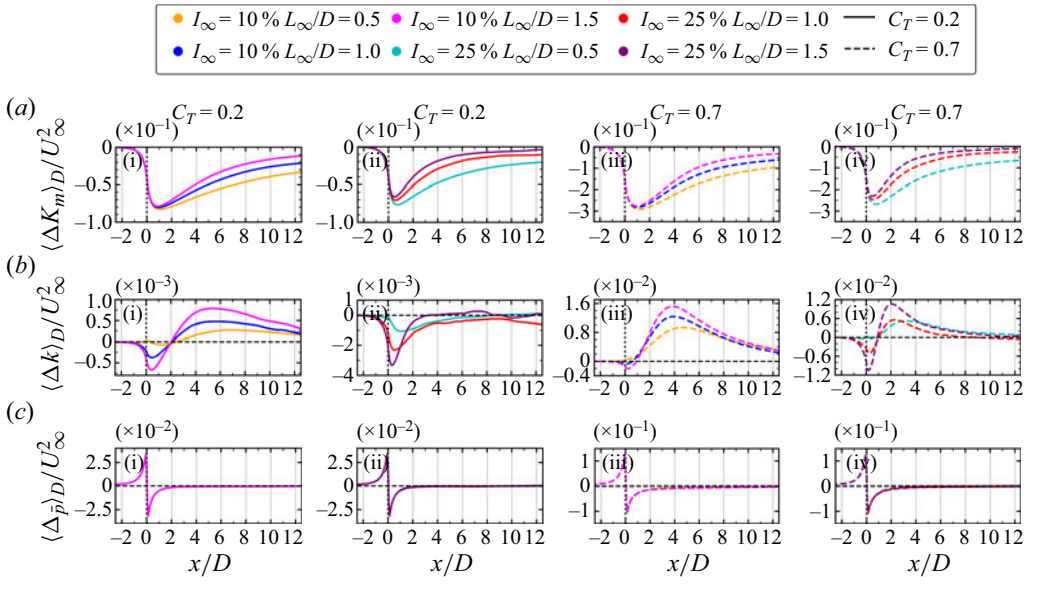

Figure 21. Time- and disk-averaged $\langle \Delta K_m \rangle_D/U_\infty^2$ (*a* i–iv), $\langle \Delta k \rangle_D/U_\infty^2$ (*b* i–iv) and ΔP_D (*c* i–iv), with (*a* i,ii,*b* i,ii,*c* i,ii) for $I_\infty = 10\,\%$ and (*a* iii,iv,*b* iii,iv,*c* iii,iv) for $I_\infty = 25\,\%$, respectively. The dashed black line represents the disk position. Here solid lines, $C_T = 0.2$; dashed lines, $C_T = 0.7$.

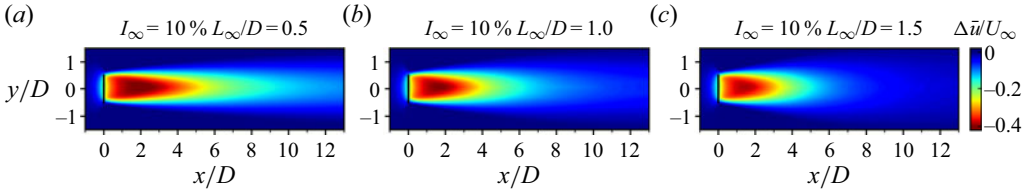

Figure 22. Contours of time-averaged streamwise velocity deficits ($\Delta\bar{u}$) for different inflow integral length scales for (*a*) $L_\infty/D = 0.5$, (*b*) $L_\infty/D = 1.0$ and (*c*) $L_\infty/D = 1.5$, respectively, with $I_\infty = 10\,\%$ and $C_T = 0.7$. The solid black lines represent the permeable disk.

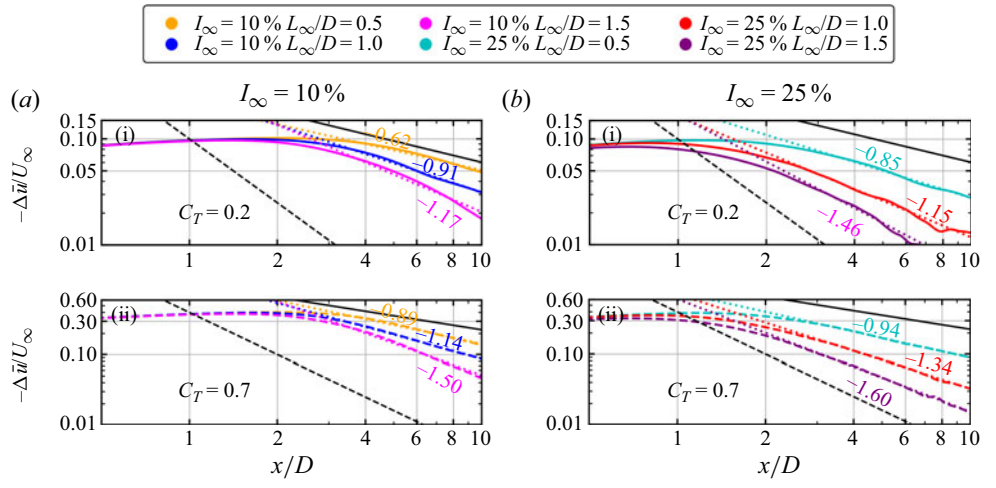

Figure 23. Variations of streamwise velocity deficits ($\Delta\bar{u}$) along wake centreline for different inflow turbulence length scales for (*a* i,ii) $I_\infty = 10\,\%$ and (*b* i,ii) $I_\infty = 25\,\%$, respectively. Here solid lines, $C_T = 0.2$; dashed lines, $C_T = 0.7$. The solid ($\sim x^{-2/3}$) and dashed ($\sim x^{-2}$) black lines represent the two limit cases: the ambient flow is non-turbulent, and the wake shear layer is the cause for flow recovery, and the wake is considered as a passive scalar with the ambient turbulence as the cause for flow recovery, respectively.

Figure 22 displays the contours of time-averaged streamwise velocity deficit ($\Delta\bar{u}$) contours on the x–y plane passing through the wake centreline. It is seen that the streamwise velocity in flow in the wake recovers faster when the inflow L_∞ is larger.

Figure 23 shows the streamwise velocity deficit along wake centreline for different inflow turbulence length scales. It is seen that the inflow L_∞ affects both the location where the velocity starts to recover and the recovery rate, especially the recovery rate. The inflow turbulence TI, on other hand, mainly affects the starting position of velocity recovery as demonstrated in § 4.1. A monotonic trend of the velocity recovery rate with the inflow TI is not observed for the wake half-width (figure 11). With the increase of L_∞, on the other hand, a monotonic increase in the velocity recovery rate is observed.

The wake half-width ($R_{1/2}/D$) is examined in figure 24. It is seen that the wake starts expansion at a location closer to the disk and expands at a higher rate when the inflow L_∞ is larger. When increasing C_T, the wake half-width becomes larger for low inflow L_∞. Comparing the impacts of the two inflow statistics shows that the inflow TI mainly affects the starting position for wake expansion, while the inflow L_∞ mainly affects the expansion rate. The wake recovery rate and the expansion rate vary with integral scale and TI, but

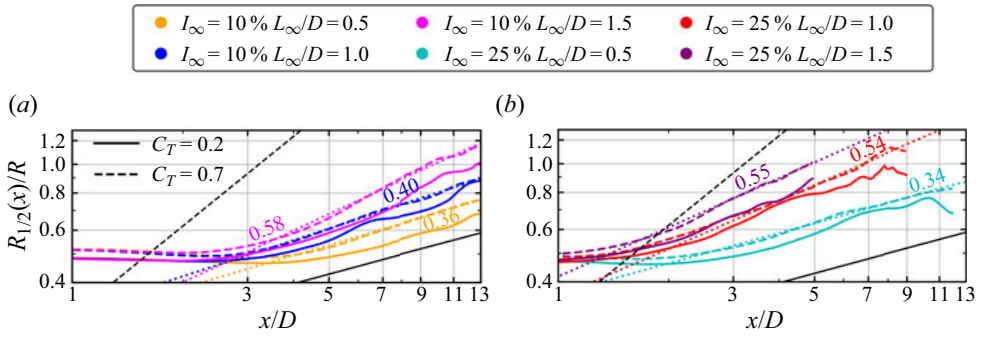

Figure 24. Streamwise variations of the time-averaged wake half-width $R_{1/2}$ for different inflow turbulence length scales for (*a*) $I_\infty = 10\,\%$, (*b*) $I_\infty = 25\,\%$, respectively. Here solid lines, $C_T = 0.2$; dashed lines, $C_T = 0.7$. The solid ($\sim x^{1/3}$) and dashed ($\sim x$) black lines represent the two limit cases: (i) the ambient flow is non-turbulent, and the wake shear layer is the cause for flow recovery, and (ii) the wake is considered as a passive scalar with the ambient turbulence as the cause for flow recovery, respectively.

both fall within the scaling ranges of the two models (George 1989; Stein & Kaltenbach 2019).

The dominant terms in the MKE budget equation are analysed in figure 25 to probe into the influence of inflow turbulence length scale L_∞ on MKE transport. It is seen that changing L_∞ mainly influences P_t, C_t and C_m terms, with negligible impacts on the T_p term, being consistent with changing inflow TI. Increasing inflow turbulence length scale increases the production of turbulence and enhances the MKE transport due to turbulence. Although changing L_∞ affects the locations of the peaks of the P_t, C_t and C_m terms, it mainly impacts their magnitude when compared with results with different inflow TIs. The $W_D + Res$ term has virtually no impact downstream of the permeable disk.

In the following, we investigate the effects of inflow turbulence length scales on the wake-added TKE (Δk). Figure 26 shows the contours of Δk on the x–y plane passing through the wake centreline. Figure 27 shows the transverse profiles of Δk at various downstream locations from the disk. It is seen that increasing the inflow turbulence length scale L_∞ increases the TKE extracted by the disk and the TKE added by the wake, with the corresponding maximum locations closer to the disk.

4.2.2. *Spectral analysis*

In this section, we investigate how inflow turbulence length scale (L_∞) affects the TKE extraction by the disk and the TKE addition by wake by carrying out spectral analysis.

We first examine the premultiplied PSD of TKE ($f\Phi_k$) along the disk edge in figures 28 and 29 for inflow $I_\infty = 10\,\%, 25\,\%$, respectively, to examine how inflow L_∞ affects wake-added TKE. It is seen in figure 28 for $I_\infty = 10\,\%$ that the wake cannot only add TKE to frequencies less than a critical one, which is approximately $St = 1.5$ for $L_\infty/D = 0.5$ and becomes $St = 2.5$ for $L_\infty/D = 1.5$. Further increasing inflow TI not only affects the intensity of wake-added TKE, but also the range of frequencies being affected, which becomes much narrower (around $0.1 < St < 1.0$), especially for high inflow L_∞ (e.g. $L_\infty/D = 1.0, 1.5$). When the inflow TI is high (i.e. $I_\infty = 25\,\%$), the ambient turbulence dominates. For relatively low inflow TI (i.e. $I_\infty = 10\,\%$), the ambient turbulence and the wake-added turbulence competes. When the peak of $f\Phi_k$ is in the range of $St \in (0.1, 1)$ (i.e. $L_\infty/D = 1.0$), the wake amplifies the peak. When the peak of $f\Phi_k$ is not within the range (on the right-hand side for $L_\infty/D = 0.5$, while on the left-hand side for $L_\infty/D =$

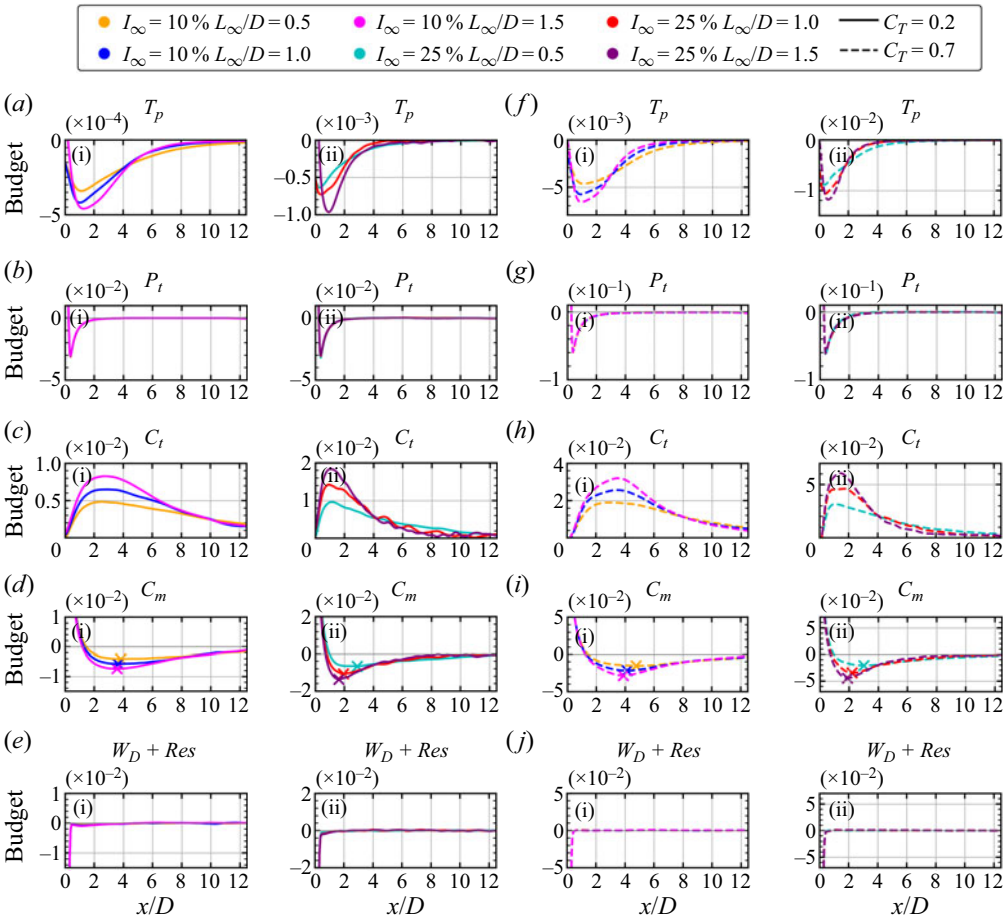

Figure 25. (*a* i,ii,*f* i,ii) Turbulence production (T_p), (*b* i,ii,*g* i,ii) pressure transport (P_t), (*c* i,ii,*h* i,ii) turbulence convection (C_t), (*d* i,ii,*i* i,ii) mean convection (C_m) and (*e* i,ii,*j* i,ii). The W_D + Res terms of the MKE budget equation for different incoming integral length scales for subpanels (i) $I_\infty = 10\,\%$ and subpanels (ii) $I_\infty = 25\,\%$. Panels (*a–e*) with solid lines, $C_T = 0.2$; (*f–j*) with dashed lines, $C_T = 0.7$. The MKE budget terms are normalized using U_∞ and D.

1.5), the wake relocates the peak (to the left-hand side for $L_\infty/D = 0.5$, while to the right-hand side for $L_\infty/D = 1.5$), with a larger relocation observed when the inflow L_∞ is smaller (i.e. $L_\infty/D = 0.5$) (for which the wake is more capable of changing because of the overall energy cascade direction).

We then examine how inflow turbulence length scale affects the disk in extracting inflow TKE in figure 30, which shows $f\Phi_k$ at $0.5D$ disk downstream and the wake centreline. It is seen that the disk is capable of extracting TKE at higher frequencies (i.e. around $St > 1.5$) for all three inflow turbulence length scales. It is capable of extracting TKE at lower frequencies (i.e. $St < 0.15$), however, it depends on the inflow turbulence length scale. For small inflow L_∞ (i.e. $L_\infty/D = 0.5$), the energy at lower frequencies barely changes. For large inflow L_∞ (i.e. $L_\infty/D = 1.5$), on the other hand, a significant amount of energy at lower frequencies is extracted by the disk. The TKE extraction at medium frequencies (i.e. $0.1 < St < 1.0$) is negligible for all the inflow turbulence length scales.

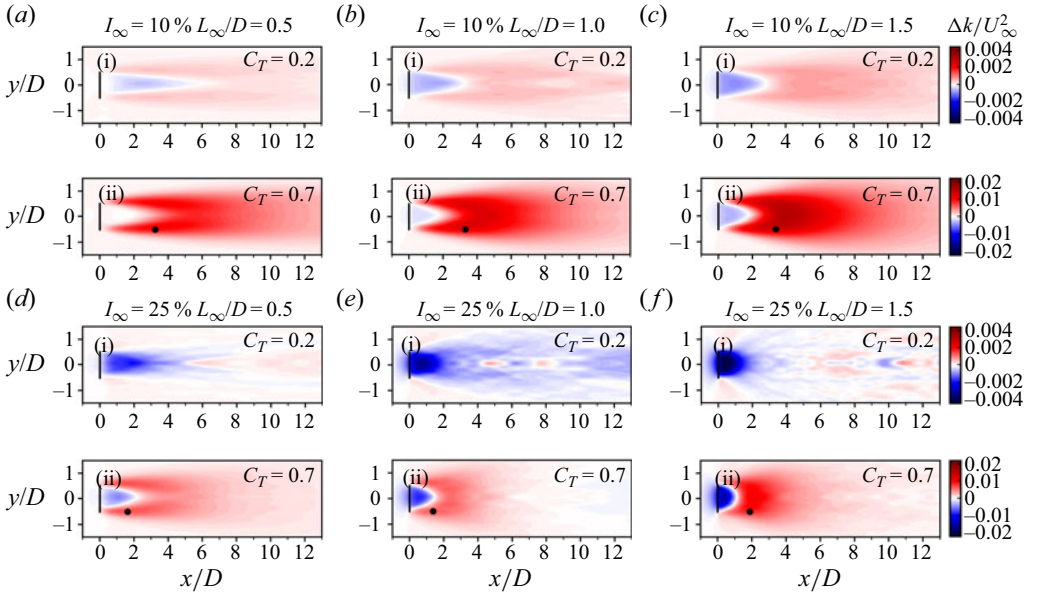

Figure 26. Contours of wake-added TKE (Δk) on the x–y plane passing through the wake centreline for different inflow turbulence length scales for (a i,ii) $I_\infty = 10\,\%$ and (b i,ii) $I_\infty = 25\,\%$, respectively. The solid black lines represent the permeable disk. The black dots indicate the positions with the maximum wake-added TKE at the edge region of the permeable disk. Here solid lines, $C_T = 0.2$; dashed lines, $C_T = 0.7$.

The TKE extraction at the disk and the TKE generation in the wake are influenced in scale space by inflow turbulence length scales (L_∞) which are examined in figure 31, which shows the energy density difference ΔE on the x–s plane for different inflow L_∞. As seen, changing the inflow L_∞ does not change the overall energy distribution, but influences the extents of energy extraction and addition, which are greater with the maximum ΔE located closer to the disk when the inflow L_∞ is larger. Figure 32 shows the curves of premultiplied energy density difference $\Delta(sE)$ at several streamwise locations. The impact of inflow turbulence length scale (L_∞) is demonstrated more clearly. It is seen that changing the inflow L_∞ does not influence the shape of the $\Delta(sE)$ distribution with the peak for TKE extraction and TKE addition located at approximately $s = 2.0D$ and $s = 1.0D$, respectively, and the starting scale with energy extraction around $s = 0.5D$. The major effect of increasing inflow L_∞ is on the enhancement of TKE extraction and addition.

4.2.3. *Quadrant analysis*

The quadrant analysis results from the cases with different inflow length scales are shown in figures 33 and 34. Impacts of the wake on the quadrant contributions similar to the cases with varying inflow TI are observed, that the intensities of the events are enhanced in quadrants $Q2$ and $Q4$, while are weakened in $Q1$ and $Q3$, making S_2 and S_4 dominant over S_1 and S_3. Moreover, it is seen that the reductions in $Q1$ and $Q3$ events (i.e. ΔS_1 and ΔS_3) and the enhancements in $Q2$ and $Q4$ events (i.e. ΔS_2 and ΔS_3) are larger at $x/D \sim 1.0$ and $x/D \sim 3.0$, respectively, and increase with the inflow integral length scale L_∞. Two differences can be identified for the effects of inflow L_∞ and I_∞: (i) varying I_∞ affects the locations of wake-induced $\Delta S_j (j = 1 - 4)$, while varying L_∞ mainly affects

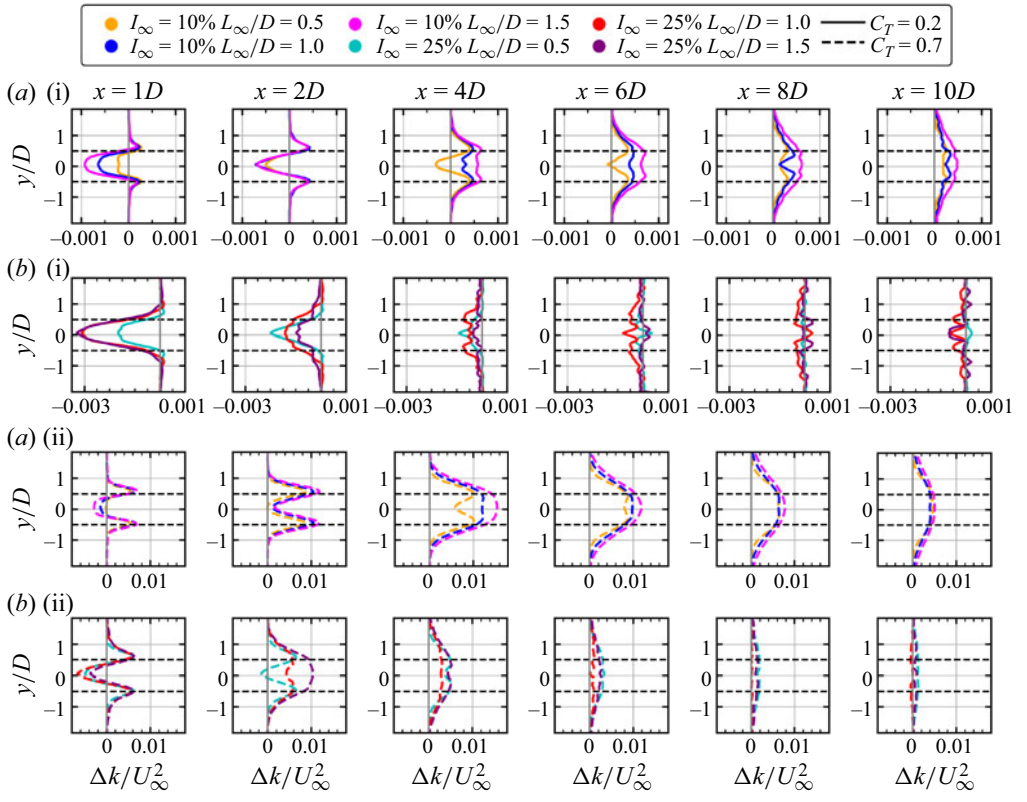

Figure 27. Transverse profiles of wake-added TKE (Δk) at different disk downstream locations for different inflow turbulence length scales for (*a* i,ii) $I_\infty = 10\,\%$ and (*b* i,ii) $I_\infty = 25\,\%$, respectively. The horizontal black dotted lines at $y/D = \pm 0.5$ denote the tip locations. Here solid lines, $C_T = 0.2$; dashed lines, $C_T = 0.7$.

the magnitude; (ii) varying I_∞ affects the relative contributions from $Q2$ and $Q4$ events, while varying L_∞ barely does.

5. Conclusions

In this work, we systematically investigated how the inflow TI, I_∞, and integral length scale, L_∞, affect the flow recovery in the wake, the capability of a permeable disk in extracting inflow TKE and the statistics of wake-added TKE using LES. Various turbulent inflows were considered, including turbulence intensities from $I_\infty = 2.5\,\%$ to $25\,\%$ with integral length scales from $L_\infty/D = 0.5$ to 2.0. The thrust coefficient is $C_T = 0.7$ for most inflows, and $C_T = 0.2$ for some inflows.

The simulation results show that the inflow turbulence affects flow recovery in the wake in two aspects, i.e. the location where the wake flow starts to recover and the rate at which it recovers. Both inflow TI and length scale affect the two aspects, with the former playing a more important role in affecting the starting location and the latter mainly affecting the recovery rate. Specifically, it was found that increasing inflow TI promotes the wake to recover at locations close to the disk, and increasing the inflow length scale increases the wake recovery rate. Quadrant analyses were carried out. It was shown that the ejections and sweeps in the quadrant $Q2$ and $Q4$ are enhanced because of the disk wake, making the two the dominant factors for wake recovery and turbulence generation. Increasing inflow

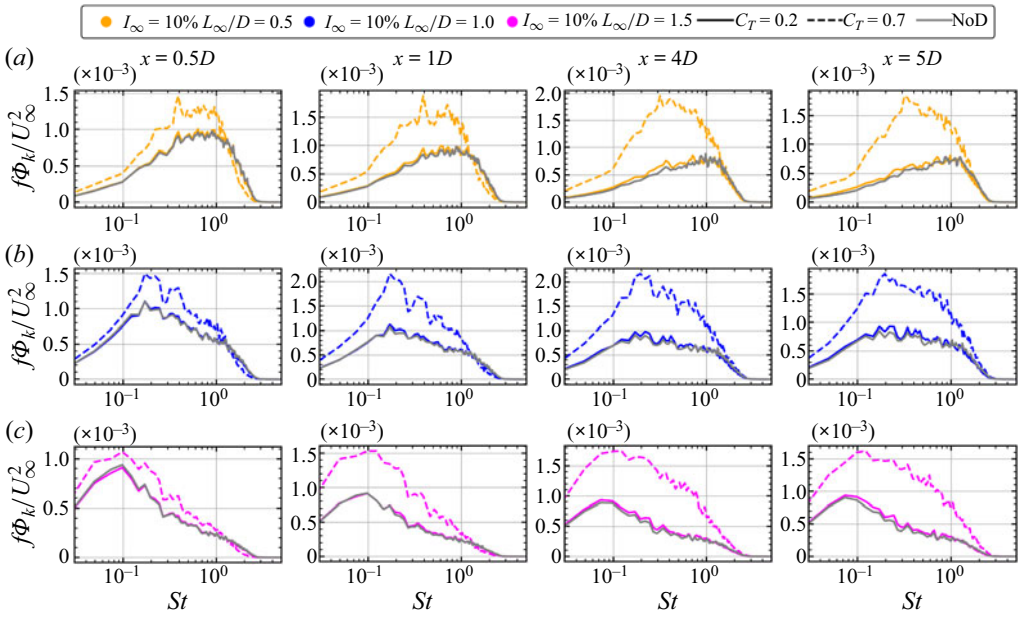

Figure 28. Premultiplied PSD of TKE at streamwise locations along the disk edge for different inflow length scales with inflow $I_\infty = 10\,\%$: (*a*) $L_\infty/D = 0.5$; (*b*) $L_\infty/D = 1.0$; (*c*) $L_\infty/D = 1.5$. Here solid lines, $C_T = 0.2$; dashed lines: $C_T = 0.7$. The grey lines represent the data for background flow.

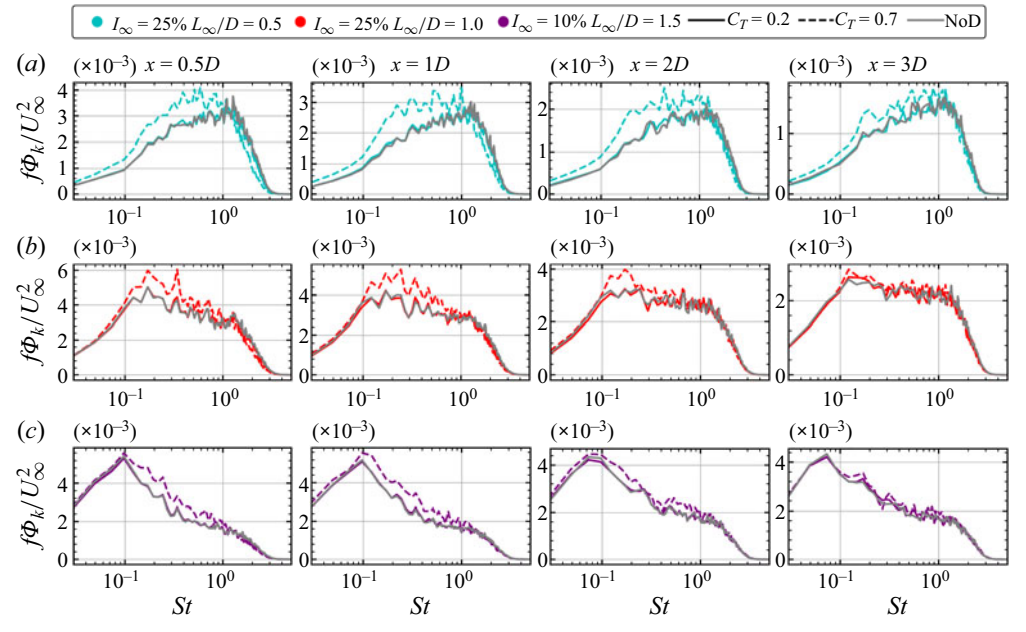

Figure 29. Premultiplied PSD of TKE at streamwise locations along the disk edge for different inflow length scales with inflow $I_\infty = 25\,\%$: (*a*) $L_\infty/D = 0.5$; (*b*) $L_\infty/D = 1.0$; (*c*) $L_\infty/D = 1.5$. Here solid lines, $C_T = 0.2$; dashed lines, $C_T = 0.7$. The grey lines represent the data for background flow.

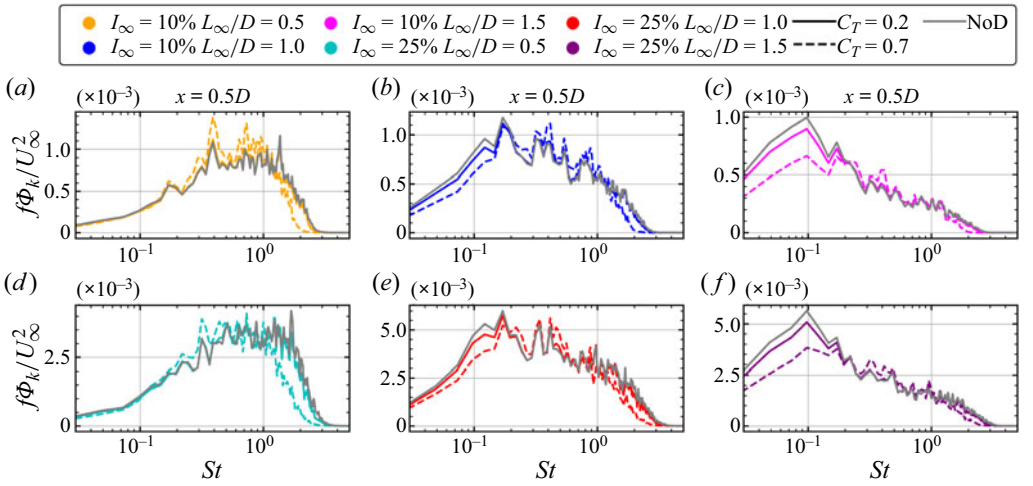

Figure 30. Premultiplied PSD of TKE at $0.5D$ disk downstream and wake centreline for different inflow length scales with inflow $I_\infty = 10, 25\,\%$: (a,d) $L_\infty/D = 0.5$; (b,e) $L_\infty/D = 1.0$; (c,f) $L_\infty/D = 1.5$. Here solid lines, $C_T = 0.2$; dashed lines, $C_T = 0.7$. The grey lines represent the data for background flow.

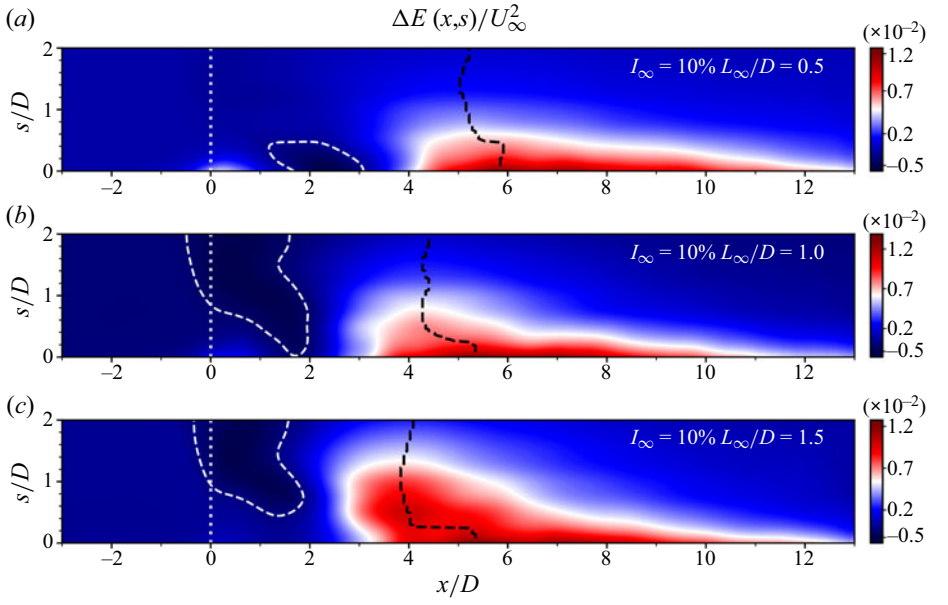

Figure 31. Contours of energy density difference $\Delta E(x, s)$ on the x–s plane for (a) $L_\infty/D = 0.5$, (b) $L_\infty/D = 1.0$ and (c) $L_\infty/D = 1.5$ with $I_\infty = 10\,\%$ and $C_T = 0.7$. The white dashed line corresponds to 0.25 times the maximum TKE loss value. The black dashed line is the peak of energy density in the streamwise location for each scale. The vertical black dotted line indicates the location of permeable disk.

TI and integral length scale increase the magnitudes of enhancements of the $Q2$ and $Q4$ events, with the former relocating the maximum enhancement location towards the disk.

A permeable disk can extract a part of TKE of the incoming flow. The simulation results show that the extent of TKE extraction and the frequencies and scales at which the TKE is extracted depends on both the inflow TI and turbulence length scale. It was found that

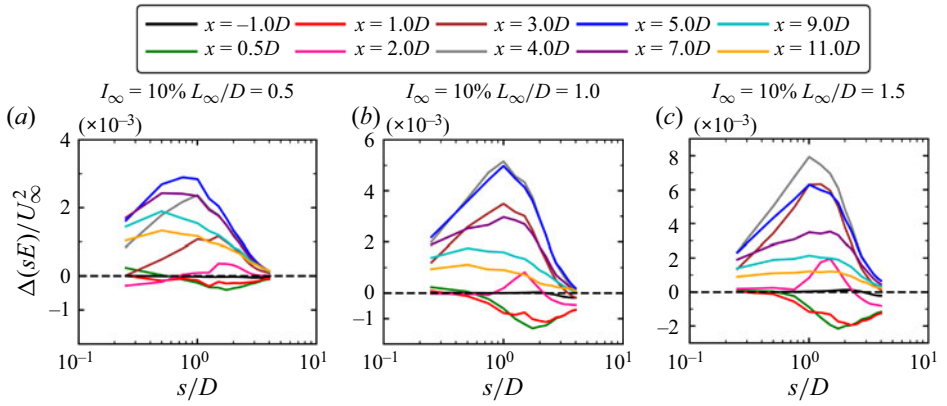

Figure 32. Premultiplied energy density difference (ΔsE) in scale space (s) at different streamwise locations for (a) $L_\infty/D = 0.5$, (b) $L_\infty/D = 1.0$ and (c) $L_\infty/D = 1.5$ with $I_\infty = 10\,\%$ and $C_T = 0.7$.

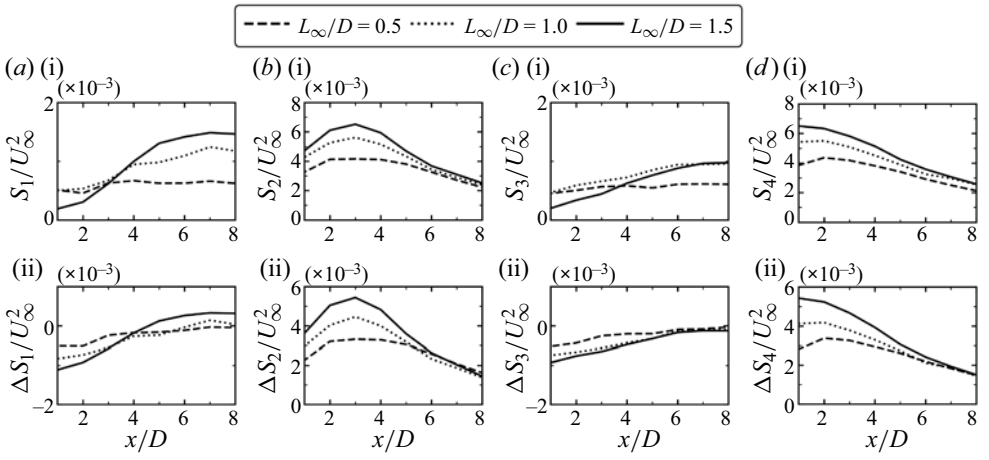

Figure 33. Quadrant analysis for cases with different inflow length scales for (a i,b i,c i,d i) contributions in each quadrant (S_i/U_∞^2), (a ii,b ii,c ii,d ii) wake-added difference in each quadrant ($\Delta S_i/U_\infty^2$). The inflow integral TI is $I_\infty = 10\,\%$. The thrust coefficient is $C_T = 0.7$.

increasing the inflow TI and length scale increases the maximum TKE extraction. The range of frequencies for TKE extraction mainly depends on the inflow length scale: at higher frequencies with $St > 1.5$ for small inflow length scale ($L_\infty/D = 0.5$); at both higher frequencies with $St > 1.5$ and lower frequencies with $St < 0.15$ for medium inflow length scale ($L_\infty/D = 1.0$); and at lower frequencies with $St < 0.15$ for larger inflow length scale ($L_\infty/D = 1.5$). The spectral analysis in scale space showed that the TKE extraction happens at larger scales with $s > 0.5D$ with peak located around $s = 2.0D$, with an exception that it occurs at almost all scales for the high inflow TI case with $I_\infty = 25\,\%$.

The shear layer in the wake adds TKE to the wake flow. The simulation results show that both inflow TI and turbulence length scale affect the intensity of wake-added TKE and the location for the maximum wake-added TKE. Specifically, it was found that increasing inflow TI and turbulence length scale promotes the maximum wake-added TKE to occur at locations close to the disk. As for the intensity of wake-added TKE, a higher inflow TI (e.g. $I_\infty = 25\,\%$) results in a lower TKE increase, while a larger inflow turbulence length scale

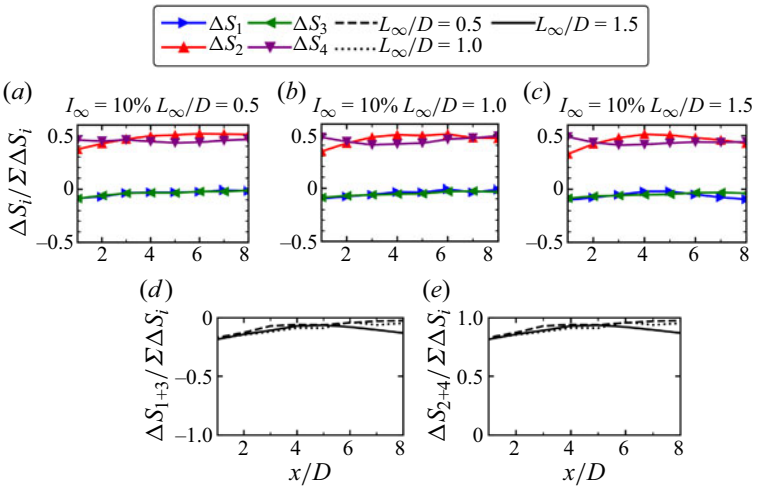

Figure 34. (*a–c*) Wake-added relative contributions in each quadrant ($\Delta S_i/\sum \Delta S_i$), (*d*) wake-added relative contributions in $Q1$ and $Q3$ events and (*e*) wake-added relative contributions in $Q2$ and $Q4$ events with different inflow length scales. The inflow integral TI is $I_\infty = 10\,\%$. The thrust coefficient is $C_T = 0.7$.

(e.g. $L_\infty/D = 1.5$) is correlated with a higher TKE increase. The range of frequencies at which the wake can add TKE is mainly affected by the inflow TI, which is wide for low inflow TI (e.g. $St < 2.0$ for $I_\infty = 2.5\,\%$) and narrow for high inflow TI (e.g. $0.1 < St < 1.0$ for $I_\infty = 25\,\%$). The inflow turbulence length scale, on the other hand, can affect the dominant frequency. When the dominant frequency of the inflow turbulence is not in the range of $0.1 < St < 1.0$ (i.e. $L_\infty/D = 0.5$, 1.5), the wake-added turbulence will attempt to allocate the peak to the mentioned range. Spectral analysis in scale space showed similar distributions of wake-added premultiplied energy density with the maximum around $s = 1.0D$ independent of inflow TI and turbulence length scale.

Neglecting the effect of wind shear simplifies the analysis, in the meantime, it is also a limitation of this study. Further in-depth spatiotemporal turbulence analyses (He, Jin & Yang 2017) carefully accounting for the effects from wind shear are necessary. The complex impacts of inflow turbulence on wake statistics pose challenges to Reynolds-averaged Navier–Stokes models (Zehtabiyan-Rezaie & Abkar 2024), that further development to account for such effects is necessary.

Supplementary movies. Supplementary movies are available at https://doi.org/10.1017/jfm.2024.876.

Funding. This work was supported by NSFC Basic Science Center Program for 'Multiscale Problems in Nonlinear Mechanics' (no. 11988102), the Strategic Priority Research Program, Chinese Academy of Sciences (CAS) (no. XDB0620102), National Natural Science Foundation of China (nos. 12172360 and 12202453) and the CAS Project for Young Scientists in Basic Research (YSBR-087).

Declaration of interests. The authors report no conflict of interest.

Author ORCIDs.
Yunliang Li https://orcid.org/0009-0004-9944-1822;
Fengshun Zhang https://orcid.org/0000-0002-2885-9947;
Zhaobin Li https://orcid.org/0000-0003-2224-7074;
Xiaolei Yang https://orcid.org/0000-0002-2606-0672.

Integral length scale (L_∞)	Thrust coefficient (C_T)	$I_\infty = 10\,\%$	$I_\infty = 25\,\%$
$L_\infty/D = 0.5$	$C_T = 0.2$	0.974	0.995
	$C_T = 0.7$	0.988	0.999
$L_\infty/D = 1.0$	$C_T = 0.2$	0.992	0.987
	$C_T = 0.7$	0.997	0.998
$L_\infty/D = 1.5$	$C_T = 0.2$	0.980	0.986
	$C_T = 0.7$	0.991	0.997

Table 2. The R^2 for velocity deficit fitting: the data from $3D$ to $10D$ permeable disk downwind positions are employed for fitting.

Integral length scale (L_∞)	Thrust coefficient (C_T)	$I_\infty = 2.5\,\%$	$I_\infty = 10\,\%$	$I_\infty = 25\,\%$
$L_\infty/D = 0.5$	$C_T = 0.7$	—	0.989	0.993
$L_\infty/D = 1.0$	$C_T = 0.7$	0.999	0.995	0.982
$L_\infty/D = 1.5$	$C_T = 0.7$	—	0.992	0.993

Table 3. The R^2 for wake half-width fitting: the data from $3D$ to $10D$ permeable disk downwind positions are employed for fitting except for the $I_\infty = 2.5\,\%$ case, for which the starting position is $6D$.

Appendix A

The optimize.curve_fit() function in Python was employed for curve fitting. The range of disk downstream positions employed for curve fitting is shown in tables 2 and 3. The R-square (i.e. R^2) is employed to measure the goodness of fit, which is in the following form:

$$R^2 = 1 - \frac{\sum_{i=0}^{n}(y_i - \hat{y})^2}{\sum_{i=0}^{n}(y_i - \bar{y})^2}, \tag{A1}$$

where y represents the data to be fitted with the mean value denoted $\bar{y}$, the fitted data $\hat{y}$, and n the size of the data. As seen in the tables, the value of R^2 is greater than 0.97 for all the considered cases.

References

Abkar, M. & Porté-Agel, F. 2015 Influence of atmospheric stability on wind-turbine wakes: a large-eddy simulation study. *Phys. Fluids* **27** (3), 035104.

Barlas, E., Buckingham, S. & van Beeck, J.P.A.J. 2016 Roughness effects on wind-turbine wake dynamics in a boundary-layer wind tunnel. *Boundary-Layer Meteorol.* **158**, 27–42.

Bastankhah, M. & Porté-Agel, F. 2016 Experimental and theoretical study of wind turbine wakes in yawed conditions. *J. Fluid Mech.* **806**, 506–541.

Blackmore, T., Batten, W.M.J. & Bahaj, A.S. 2014 Influence of turbulence on the wake of a marine current turbine simulator. *Proc. R. Soc.* A **470** (2170), 20140331.

Carbajo Fuertes, F., Markfort, C.D. & Porté-Agel, F. 2018 Wind turbine wake characterization with nacelle-mounted wind lidars for analytical wake model validation. *Remote Sens.* **10** (5), 668.

Chamorro, L.P., Guala, M., Arndt, R.E.A. & Sotiropoulos, F. 2012 On the evolution of turbulent scales in the wake of a wind turbine model. *J. Turbul.* **13**, N27.

Cortina, G., Calaf, M. & Cal, R.B. 2016 Distribution of mean kinetic energy around an isolated wind turbine and a characteristic wind turbine of a very large wind farm. *Phys. Rev. Fluids* **1** (7), 074402.

Dong, G., Li, Z., Qin, J. & Yang, X. 2022 How far the wake of a wind farm can persist for? *Theor. Appl. Mech. Lett.* **12** (1), 100314.

DONG, G., QIN, J., LI, Z. & YANG, X. 2023 Characteristics of wind turbine wakes for different blade designs. *J. Fluid Mech.* **965**, A15.
GAMBUZZA, S. & GANAPATHISUBRAMANI, B. 2021 The effects of free-stream turbulence on the performance of a model wind turbine. *J. Renew. Sustain. Energy* **13** (2), 023304.
GAMBUZZA, S. & GANAPATHISUBRAMANI, B. 2023 The influence of free stream turbulence on the development of a wind turbine wake. *J. Fluid Mech.* **963**, A19.
GE, L. & SOTIROPOULOS, F. 2007 A numerical method for solving the 3d unsteady incompressible Navier–Stokes equations in curvilinear domains with complex immersed boundaries. *J. Comput. Phys.* **225** (2), 1782–1809.
GE, M., ZHANG, S., MENG, H. & MA, H. 2020 Study on interaction between the wind-turbine wake and the urban district model by large eddy simulation. *Renew. Energy* **157**, 941–950.
GEORGE, W.K. 1989 The self-preservation of turbulent flows and its relation to initial conditions and coherent structures. *Adv. Turbul.* **3973**, 39–73.
GERMANO, M., PIOMELLI, U., MOIN, P. & CABOT, W.H. 1991 A dynamic subgrid-scale eddy viscosity model. *Phys. Fluids* A **3** (7), 1760–1765.
GHATE, A.S., GHAISAS, N., LELE, S.K. & TOWNE, A. 2018 Interaction of small scale homogenenous isotropic turbulence with an actuator disk. In *2018 Wind Energy Symposium*, p. 0753.
HE, G., JIN, G. & YANG, Y. 2017 Space-time correlations and dynamic coupling in turbulent flows. *Annu. Rev. Fluid Mech.* **49**, 51–70.
HEISEL, M., HONG, J. & GUALA, M. 2018 The spectral signature of wind turbine wake meandering: a wind tunnel and field-scale study. *Wind Energy* **21** (9), 715–731.
ISHIHARA, T. & QIAN, G.-W. 2018 A new Gaussian-based analytical wake model for wind turbines considering ambient turbulence intensities and thrust coefficient effects. *J. Wind Engng Ind. Aerodyn.* **177**, 275–292.
IVANELL, S., MIKKELSEN, R., SØRENSEN, J.N. & HENNINGSON, D. 2010 Stability analysis of the tip vortices of a wind turbine. *Wind Energy* **13** (8), 705–715.
JIN, Y., LIU, H., AGGARWAL, R., SINGH, A. & CHAMORRO, L.P. 2016 Effects of freestream turbulence in a model wind turbine wake. *Energies* **9** (10), 830.
KANKANWADI, K.S. & BUXTON, O.R.H. 2020 Turbulent entrainment into a cylinder wake from a turbulent background. *J. Fluid Mech.* **905**, A35.
KNOLL, D.A. & KEYES, D.E. 2004 Jacobian-free Newton–Krylov methods: a survey of approaches and applications. *J. Comput. Phys.* **193** (2), 357–397.
LI, Z., DONG, G. & YANG, X. 2022 Onset of wake meandering for a floating offshore wind turbine under side-to-side motion. *J. Fluid Mech.* **934**, A29.
LI, Z. & YANG, X. 2021 Large-eddy simulation on the similarity between wakes of wind turbines with different yaw angles. *J. Fluid Mech.* **921**, A11.
LI, Z. & YANG, X. 2024 Resolvent-based motion-to-wake modelling of wind turbine wakes under dynamic rotor motion. *J. Fluid Mech.* **980**, A48.
LISSAMAN, P.B.S. 1979 Energy effectiveness of arbitrary arrays of wind turbines. *J. Energy* **3** (6), 323–328.
LIU, X., LI, Z., YANG, X., XU, D., KANG, S. & KHOSRONEJAD, A. 2022 Large-eddy simulation of wakes of waked wind turbines. *Energies* **15** (8), 2899.
MANN, J. 1998 Wind field simulation. *Probab. Engng Mech.* **13** (4), 269–282.
MAO, X. & SØRENSEN, J.N. 2018 Far-wake meandering induced by atmospheric eddies in flow past a wind turbine. *J. Fluid Mech.* **846**, 190–209.
MARTINEZ-TOSSAS, L.A., CHURCHFIELD, M.J., YILMAZ, A.E., SARLAK, H., JOHNSON, P.L., SØRENSEN, J.N., MEYERS, J. & MENEVEAU, C. 2018 Comparison of four large-eddy simulation research codes and effects of model coefficient and inflow turbulence in actuator-line-based wind turbine modeling. *J. Renew. Sustain. Energy* **10** (3), 033301.
MENEVEAU, C. 2019 Big wind power: seven questions for turbulence research. *J. Turbul.* **20** (1), 2–20.
MENEVEAU, C., LUND, T.S. & CABOT, W.H. 1996 A lagrangian dynamic subgrid-scale model of turbulence. *J. Fluid Mech.* **319**, 353–385.
MEYERS, J. & MENEVEAU, C. 2013 Flow visualization using momentum and energy transport tubes and applications to turbulent flow in wind farms. *J. Fluid Mech.* **715**, 335–358.
SAAD, Y. 1993 A flexible inner-outer preconditioned GMRES algorithm. *SIAM J. Sci. Comput.* **14** (2), 461–469.
SARLAK, H., MENEVEAU, C. & SØRENSEN, J.N. 2015 Role of subgrid-scale modeling in large eddy simulation of wind turbine wake interactions. *Renew. Energy* **77**, 386–399.
SCHLICHTING, H. & GERSTEN, K. 2016 *Boundary-Layer Theory*. Springer.

SIROVICH, L. 1987 Turbulence and the dynamics of coherent structures. I. Coherent structures. *Q. Appl. Maths* **45** (3), 561–571.

SØRENSEN, J.N. 2011 Aerodynamic aspects of wind energy conversion. *Annu. Rev. Fluid Mech.* **43**, 427–448.

ST MARTIN, C.M., LUNDQUIST, J.K., CLIFTON, A., POULOS, G.S. & SCHRECK, S.J. 2016 Wind turbine power production and annual energy production depend on atmospheric stability and turbulence. *Wind Energy Sci.* **1** (2), 221–236.

STEIN, V.P. & KALTENBACH, H.-J. 2019 Non-equilibrium scaling applied to the wake evolution of a model scale wind turbine. *Energies* **12** (14), 2763.

STEVENS, R.J.A.M. & MENEVEAU, C. 2017 Flow structure and turbulence in wind farms. *Annu. Rev. Fluid Mech.* **49**, 311–339.

TALAVERA, M. & SHU, F. 2017 Experimental study of turbulence intensity influence on wind turbine performance and wake recovery in a low-speed wind tunnel. *Renew. Energy* **109**, 363–371.

VAHIDI, D. & PORTÉ-AGEL, F. 2022 A physics-based model for wind turbine wake expansion in the atmospheric boundary layer. *J. Fluid Mech.* **943**, A49.

VEERS, P., *et al.* 2019 Grand challenges in the science of wind energy. *Science* **366** (6464), eaau2027.

VERMEER, L.J., SØRENSEN, J.N. & CRESPO, A. 2003 Wind turbine wake aerodynamics. *Prog. Aerosp. Sci.* **39** (6–7), 467–510.

WALLACE, J.M. 2016 Quadrant analysis in turbulence research: history and evolution. *Annu. Rev. Fluid Mech.* **48**, 131–158.

WALLACE, J.M., ECKELMANN, H. & BRODKEY, R.S. 1972 The wall region in turbulent shear flow. *J. Fluid Mech.* **54** (1), 39–48.

WANG, Z., DONG, G., LI, Z. & YANG, X. 2023 Statistics of wind farm wakes for different layouts and ground roughness. *Boundary-Layer Meteorol.* **188**, 285–320.

WU, Y.-T. & PORTÉ-AGEL, F. 2012 Atmospheric turbulence effects on wind-turbine wakes: an LES study. *Energies* **5** (12), 5340–5362.

YANG, X., HOWARD, K.B., GUALA, M. & SOTIROPOULOS, F. 2015*a* Effects of a three-dimensional hill on the wake characteristics of a model wind turbine. *Phys. Fluids* **27** (2), 025103.

YANG, X., KANG, S. & SOTIROPOULOS, F. 2012 Computational study and modeling of turbine spacing effects in infinite aligned wind farms. *Phys. Fluids* **24** (11), 115107.

YANG, X. & SOTIROPOULOS, F. 2013 On the predictive capabilities of les-actuator disk model in simulating turbulence past wind turbines and farms. In *2013 American Control Conference*, pp. 2878–2883. IEEE.

YANG, X. & SOTIROPOULOS, F. 2018 A new class of actuator surface models for wind turbines. *Wind Energy* **21** (5), 285–302.

YANG, X. & SOTIROPOULOS, F. 2019 Wake characteristics of a utility-scale wind turbine under coherent inflow structures and different operating conditions. *Phys. Rev. Fluids* **4** (2), 024604.

YANG, X., SOTIROPOULOS, F., CONZEMIUS, R.J., WACHTLER, J.N. & STRONG, M.B. 2015*b* Large-eddy simulation of turbulent flow past wind turbines/farms: the virtual wind simulator (VWiS). *Wind Energy* **18** (12), 2025–2045.

ZEHTABIYAN-REZAIE, N. & ABKAR, M. 2024 An extended k–ε model for wake-flow simulation of wind farms. *Renew. Energy* **222**, 119904.

ZHANG, F., YANG, X. & HE, G. 2023 Multiscale analysis of a very long wind turbine wake in an atmospheric boundary layer. *Phys. Rev. Fluids* **8** (10), 104605.